



This is a repository copy of *Transition between tangential and co-axial liquid crystalline honeycombs in the self-assembly of Y-shaped bolapolyphiles*.

White Rose Research Online URL for this paper:
<http://eprints.whiterose.ac.uk/139366/>

Version: Accepted Version

Article:

Lehmann, A., Prehm, M., Chen, C. et al. (4 more authors) (2018) Transition between tangential and co-axial liquid crystalline honeycombs in the self-assembly of Y-shaped bolapolyphiles. *Chemical Communications*, 54 (87). pp. 12306-12309. ISSN 1359-7345

<https://doi.org/10.1039/c8cc06281a>

© 2018 The Royal Society of Chemistry. This is an author produced version of a paper subsequently published in *Chemical Communications*. Uploaded in accordance with the publisher's self-archiving policy.

Reuse

Items deposited in White Rose Research Online are protected by copyright, with all rights reserved unless indicated otherwise. They may be downloaded and/or printed for private study, or other acts as permitted by national copyright laws. The publisher or other rights holders may allow further reproduction and re-use of the full text version. This is indicated by the licence information on the White Rose Research Online record for the item.

Takedown

If you consider content in White Rose Research Online to be in breach of UK law, please notify us by emailing eprints@whiterose.ac.uk including the URL of the record and the reason for the withdrawal request.



eprints@whiterose.ac.uk
<https://eprints.whiterose.ac.uk/>

Cite this: DOI: 10.1039/c0xx00000x

www.rsc.org/xxxxxx

ARTICLE TYPE

Transition between tangential and co-axial liquid crystalline honeycombs in the self-assembly of Y-shaped bolapolyphiles

Anne Lehmann,^a Marko Prehm,^a Changlong Chen,^b Feng Liu,^{b,*} Xiangbing Zeng,^c Goran Ungar,^{c,*} Carsten Tschierske^{a,*}

⁵ Received (in XXX, XXX) Xth XXXXXXXXX 20XX, Accepted Xth XXXXXXXXX 20XX
DOI: 10.1039/b000000x

***p*-terphenyl based Y-shaped bolapolyphiles self-assemble into liquid crystalline honeycombs with co-axial organization of the π -conjugated rods around columns filled by alkyl sidechains. In this new hexagonal honeycomb with $P6/mmm$ symmetry the orientation of the π -conjugated rods is perpendicular to the tangential honeycombs formed at lower temperature or with longer chain length.**

Liquid crystals (LCs) are nowadays indispensable for display- and information technology.¹ The architecture of the industrially used LCs is relatively simple, but in the recent decades the complexity of LC molecules and their self-assembly has been significantly increased.^{1,2} Columnar LC phases, for example, were found for a wide range of molecular shapes from disc-like, via taper-shaped, and star-shaped to rod-like.^{1,3} The usual mode of organization of the mesogens in these columnar LCs is by stacking in columns, arranged on a 2d lattice, in most cases with hexagonal symmetry and embedded in the fluid continuum formed by the attached flexible chains. The orientation of the molecules is perpendicular to the columns or slightly tilted to the normal of the column long axis, as shown in Fig. 1a for the multi-chain (polycatenar⁴) rod-like molecules. In the recent two decades T-shaped and X-shaped polyphiles have paved the way to new modes of columnar self-assembly, namely the LC honeycombs, having an inverted structure with the flexible chains inside the columns and the nano-segregated rod-like mesogens forming the framework around them (Fig. 1c). In these liquid honeycombs the ratio of the volume of the alkyl chains to the length of the rods determines the number of rods arranged in the polygonal circumference of each alkyl-filled cell.^{5,6,7} The orientation of the mesogens is perpendicular to the column axis⁶ or tilted.⁸ Only recently have the co-axial rod-bundle phases, with the molecules parallel to z , been reported (Fig. 1b).⁹ Herein we report a structure (Fig. 1d) with π -conjugated rods oriented co-axially in honeycombs, thus being inverted to structures (b) and (c) in Fig. 1 either with respect to the position or orientation of the rods, respectively. This mode of honeycomb self-assembly with co-axial rods was observed for the *p*-terphenyl based compounds **An** with two polar glycerol end groups and a peripheral lateral chain (see formula in Table 1). These compounds were synthesized as described in the ESI (Scheme S1†) and their data are collated in Table 1.

Lamellar LC phases (SmA+) are dominant in most **An** compounds ($n = 5$ -13) and additional non-lamellar LC phases can

be observed for all compounds with $n \geq 8$. For compound **A11**, as a representative example, optical micrographs taken between crossed polarizers are shown in Fig. 2. The lamellar LC phase (SmA+) has a typical birefringent fan-like texture (Fig. 2a). On cooling the birefringence increases (green to second order orange) due to an increasing orientational order parameter of the rods, and at the next transition a highly viscous mosaic-like texture develops (Fig. 2b), indicative of layer stiffening in the phase designated as $P6/mmm$. At the subsequent phase transition to the low temperature (LT) phase ($p4mm$) the mosaics become broken and fluid again, accompanied by a significant decrease in birefringence (color change from 2nd order orange via 1st order green to blue, see Fig. 2c), meaning that either the degree of order or the orientation mode of the π -conjugated rods had changed.

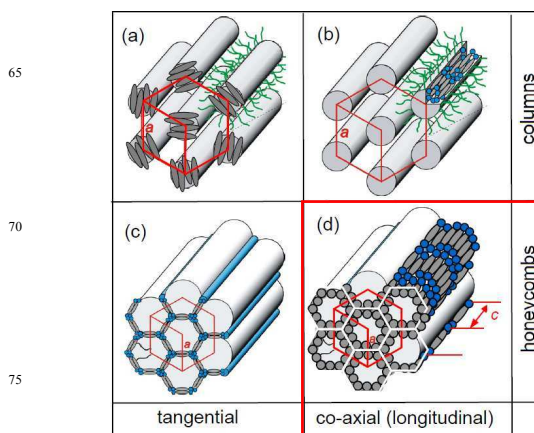
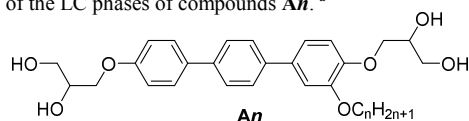


Figure 1. Hexagonal columnar organizations in LC phases. (a) formed by polycatenar molecules⁴ and (b-d) formed by bolapolyphiles with lateral chains; (b) co-axial rod-bundle phase;⁹ (c) tangential hexagonal honeycomb,⁶ and (d) the co-axial honeycomb ($P6/mmm$) reported herein.

In homeotropically aligning cells smectic layers form parallel to the surfaces. In this case the lamellar phase (SmA+), appearing at the highest temperature, is completely dark between crossed polarizers. This indicates that, on average, the terphenyls are perpendicular to the layers. Under these conditions the phase transition to the next LC phase ($P6/mmm$) is difficult to recognize; the texture remains dark and only the viscosity increases (Fig. S2a, b†). This is the first hint that another optically uniaxial mesophase has formed. A low birefringent (gray) “spherulitic” texture, typical of columnar phases, with

Table 1. Phase transitions and lattice parameters of the LC phases of compounds **An**.^a

An	Phase transitions $T/^\circ\text{C}$ [$\Delta H/\text{kJmol}^{-1}$]	SmA+: d_1, d_2 (nm)	$P6/mmm$: a_{hex}, c (nm)	$p4mm$: a_{sq} (nm)
A5	Iso 203 [6.7] SmA+ 114 [18.2] Cr	2.16, 1.83	-	-
A7	Iso 191 [6.6] SmA+ 105 [16.2] Cr	n.d.	-	-
A8	Iso 187 [6.0] SmA+ 116 [0.8] $P6/mmm$ 101 [18.1] Cr	2.20, 2.2	2.44, 2.20	-
A9	Iso 182 [5.2] SmA+ 130 [0.8] $P6/mmm$ 95 [-] M 65 [2.4] Cr	2.19, 2.32	2.64, 2.23	-
A10	Iso 182 [4.7] SmA+ 157 [1.0] $P6/mmm$ 115 [1.8] $\text{Col}_{\text{sq}}/p4mm$ 78 [11.3] Cr	2.13, 2.51	2.84, 2.17	2.81
A11	Iso 179 [4.0] SmA+ 164 [1.2] $P6/mmm$ 136 [2.4] $\text{Col}_{\text{sq}}/p4mm$ 84 [13.4] Cr	2.16, 2.66	3.05, 2.22	2.86
A12	Iso 178 [3.5] SmA+ 169 [1.4] $P6/mmm^b$ 131 [2.3] $\text{Col}_{\text{sq}}/p4mm$ 98 [17.1] Cr	2.14, 2.83	3.27, 2.21	2.86
A13	Iso 177 [3.0] SmA+ 172 [1.7] $P6/mmm^b$ 141 [3.2] $\text{Col}_{\text{sq}}/p4mm$ 107 [18.4] Cr	2.12, 2.84	3.28, 2.20	2.83
A14	Iso 179 [6.2] $\text{Col}_{\text{rec}}/p2gg$ 129 [26.0] Cr	-	-	7.00, 6.58 ($p2gg$) ^c

^a Values determined on cooling with rate 10 K min^{-1} by DSC (peak temperatures); abbreviations: Cr = crystalline solid, Iso = isotropic liquid, SmA+ = orthogonal lamellar phase with diffuse small angle scattering; $P6/mmm$ = 3D hexagonal LC phase with co-axial rod orientation in a hexagonal honeycombs; $\text{Col}_{\text{sq}}/p4mm$ = tangential square honeycomb LC phase; $\text{Col}_{\text{rec}}/p2gg$ = pentagonal honeycomb LC phase; M = unknown mesophase; n.d. = not determined; for transitions on heating, more details and calculations, see Tables S1 and S8†, for DSC traces, see Fig. S1† and for XRD data see Figs S7-S15 and Tables S2-S7†; ^b phase coexists with $\text{Col}_{\text{sq}}/p4mm$; ^c parameters a and b of the $\text{Col}_{\text{rec}}/p2gg$ phase.

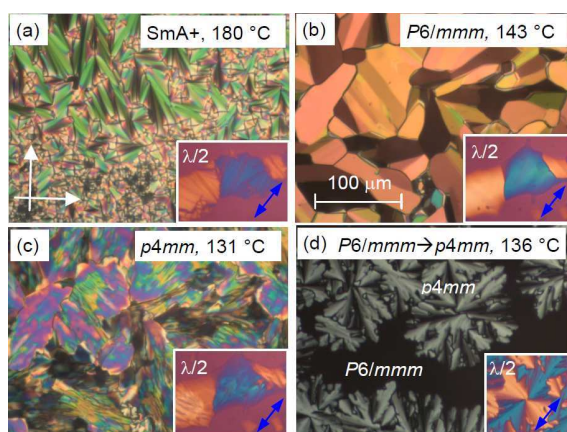


Figure 2. Textures of **A11** as observed between crossed polarizers (white arrows); a-c) in planar aligning cells (terphenyls parallel to the substrate surface, $5 \mu\text{m}$ PI coated cells) and d) in homeotropic alignment (terphenyls perpendicular to the surfaces, between non-treated microscopy glass plates) as observed on cooling. The insets show textures with additional $\lambda/2$ plate at the same temperatures, the blue arrows indicate the direction of the slow axis; for more details and explanations, see Figs. S2-S5†.

columns in the parallel to the surface, develops on further cooling at the transition to the fluid LT phase ($p4mm$, Fig. 2d).

For all **An** compounds in the whole temperature range down to crystallization, the WAXS pattern is diffuse with a maximum at $d = 0.45\text{-}0.47 \text{ nm}$, confirming true LC phases without fixed positions of individual molecules (see Section S2.3 in ESI†). In the high temperature phases of surface-aligned **A5-A13** there is a weak 1st- and a stronger 2nd-order layer reflection on the meridian, confirming a homeotropic lamellar phase with a layer thickness of $d_1 = 2.13\text{-}2.20 \text{ nm}$ (Fig. 3a and Table 1). The d -value is almost identical for all compounds and is close to the length of the bolaamphiphilic core, measured between the secondary OH groups in a compact conformation ($L_{\text{mol},\text{min}} = 2.3 \text{ nm}$, see Fig. S17a†). This indicates a smectic phase with monolayer structure. In contrast to the layer reflections, the diffuse WAXS maximum is on the equator, confirming an on average non-tilted parallel organization of terphenyls and a significant part of the alkyl chains perpendicular to the layers.

An unusual feature of this SmA+ phase is an additional diffuse scattering with relatively high intensity in the SAXS pattern (SmA+). In a homeotropically aligned sample with the X-ray beam parallel to the layers (Figs. 3a and S8b†) the maximum of this diffuse scattering (d_2) is on the equator, i.e. perpendicular to the layer reflection. It indicates additional strong short range in-plane density fluctuations with a mean distance between 1.8 and 2.8 nm. This distance increases with alkyl chain length (Table 1). This extra feature is likely to be due to the average distance between domains arising from local segregation of the flexible lipophilic alkyl chains from the polar and rigid bolaamphiphilic cores. The volume fraction of the lateral chains increases from 0.20 to 0.39 between **A5** to **A13** (Table S8†), thus the chains represent the minor component in all cases. This phase, designated as SmA+,^{5,6} can thus be considered as a mesh phase^{10,11} with the layers irregularly penetrated by alkyl chain domains. The relatively small meridional spread of the diffuse SAXS maxima on the equator suggests that the alkyl domains are columns perpendicular to the layers and cutting through several of them, on average (see Fig. 4c).

At the next phase transition, observed in compounds **A8-A13**, this diffuse scattering condenses into a sharp Bragg peak on the equator (Figs. 3b and S8†) and then it can be indexed as the (100) reflection of a 3D hexagonal lattice, spacegroup $P6/mmm$, with $a_{\text{hex}} = 2.44$ to 3.18 nm (Table 1). The positions of the (100) and (200) layer reflections on the meridian are almost unchanged and become the (001) and (002) reflections of periodicity $c = 2.17\text{-}2.22 \text{ nm}$. The GISAXS pattern in Fig. 3c confirms this assignment. The positions of the diffuse equatorial WAXS maxima do not change, indicating that the orientation of p -terphenyls and alkyl chains remains parallel to the column long axis (Fig. 3b). The proposed structure, depicted in Fig. 4b, is corroborated by the reconstructed electron density (ED) map in Fig. 3d, where the alkyl chains forming infinite low ED columns (red) are arranged on a regular hexagonal lattice and are embedded in a high ED lamellar continuum (purple) with slightly modulating ED due to the alternation of glycerols and terphenyls in the penetrated layers. The ED difference between glycerols and terphenyls is small, hence the weak (00 l) reflections. The fact that

(002) is stronger than (001) (Figs. 3c and S9b†) indicates a local ED minimum in the middle of the layers, attributed to the fact that the alkyls are tethered to the ends of the terphenyl cores (note the weak modulation in diameter of alkyl columns in Fig. 3d).

The a_{hex} parameter of the $P6/mmm$ in-plane lattice increases significantly with increasing chain length, from 2.44 nm for **A8** to 3.28 nm for **A13**. This is due to the expansion of the lipophilic columns, amplified by a concomitant increase in the number of molecules per unit cell from $n_{\text{cell}} = 14$ for **A8** to 22 for **A13** (Tables 1 and S8†). The number of molecules in the lateral cross section of these honeycomb walls is $n_{\text{wall}} = 2.6\text{--}2.7$ for all compounds (for calculation, see section S2.5 in the ESI†). Thus two to three (1.7–2.7) molecules are arranged side-by-side along each of the six sides of a hexagonal cell around each alkyl column. This structure can be considered as a co-axial honeycomb (Figs. 1d and 4b), having the rod-like mesogens arranged parallel to the column axis instead of perpendicular to it, as in the previously reported tangential honeycombs (Fig. 1c).⁶ Due to this inverted organization the periodicity provided by the bolaamphiphilic core structure leads to a periodicity along the column axis (z) instead of fixing the honeycomb shape in the x - y plane.

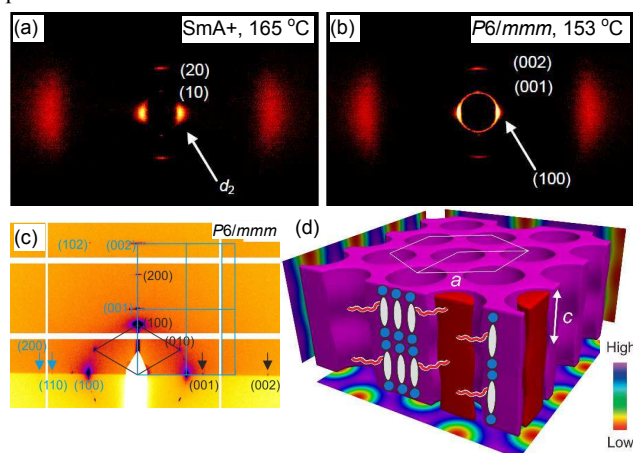


Figure 3. a,b) XRD patterns (obtained after subtraction of the scattering pattern in the isotropic liquid state, for original patterns, see Fig. S10†) of a surface aligned sample of compound **A10** in (a) SmA+ and (b) $P6/mmm$ phases; c) GISAXS pattern of the $P6/mmm$ phase of **A13** at 165 °C on a Si surface with either the (100) or the (001) axis perpendicular to the substrate surface d) electron density (ED) map of the $P6/mmm$ phase of compound **A9** (red = low ED, purple = high ED; see also Section S2.3 in the ESI†).

For compounds **A9–A13** there is an additional phase transition from $P6/mmm$ to a LT phase. Its SAXS and GISAXS patterns for compounds **A10–A13** can be indexed to a square lattice with $p4mm$ plane group (Figs. S11 and S12). The lattice parameters of the $p4mm$ phases of all four compounds are almost identical ($a_{\text{squ}} = 2.81\text{--}2.86$ nm, Table 1), being only slightly larger than the molecular length in the most stretched conformation ($L_{\text{mol,max}} = 2.6$ nm, see Fig. S17b†). This is typical of tangential honeycombs with square cells. The phase structure is corroborated by ED maps (see Figs. S11d and S14†) and is in line with the negative birefringence (see inset in Fig. 2c and Fig. S2e,f†). This confirms that the intramolecular π -conjugation pathway, i.e. the rod orientation, is perpendicular to the columns. The structure is depicted in Fig. 4a. For compounds **A12** and **A13** with longer

chains the transition from $P6/mmm$ to $p4mm$ is not complete, i.e. $p4mm$ and $P6/mmm$ coexist in the $P6/mmm$ range (Fig. S13c†). **A9** rapidly crystallizes and therefore its LT phase (M) could not be investigated. No LT phase is observed in **A8**, while even the $P6/mmm$ phase is absent in **A7** and **A5**, leaving only the SmA+ phase (Table 1, Fig. 5a). Extension of the lateral chain of **A13** by just one more CH_2 unit (**A14**) leads to a sudden and simultaneous loss of the SmA+, $P6/mmm$ and $p4mm$ phases. Only a rectangular columnar phase with $p2gg$ lattice ($a = 7.0$ nm, $b = 6.6$ nm) is left in **A14**, representing a honeycomb composed of slightly deformed pentagonal cells (Table 1, Fig. 5a, for details, see Figs. S6, S15 and S20†).

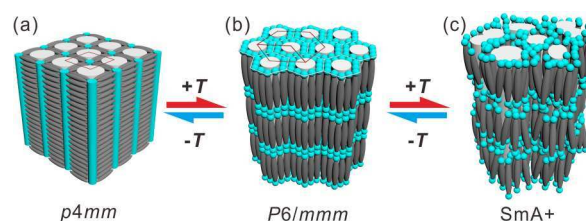


Figure 4. Schematic models of the three LC phases in compounds **An**: (a) square tangential honeycomb $p4mm$; (b) hexagonal coaxial 3D phase $P6/mmm$; (c) random mesh perforated layer phase SmA+. Grey = terphenyl, blue = glycerol, white = alkyl.

In the series of isomeric compounds **Bn** (Fig. 5b), having the lateral alkyl chain at the central benzene ring, the SmA+ phase is formed over a much smaller chain-length ($n = 5,6$) and temperature range and the $P6/mmm$ phase is completely absent.¹² Instead, **Bn** compounds exhibit a series of more conventional tangential honeycombs, as follows (Fig. 5b): a centred rectangular ($c2mm$) phase consisting of rhombic cells in **B8**; a high-temperature square $p4mm$ phase with square cells in **B9**, **B10** and **B11**, preceded in **B9–B11** at lower temperature by a rectangular $p2mm$ phase. Finally, in **B12** and **B14** we see the $p2gg$ phase made up of pentagonal cells, as in **A14**.

Why has the transfer of attachment point from the central (**Bn**) to the terminal benzene ring (**An**) caused such unusual phase behaviour in **An**? As the side-chain volume increases, either due to increased temperature or to addition of extra CH_2 groups, the squares of the $p4mm$ phase would be expected to turn into pentagons or hexagons, as in the **Bn** and other T-shaped amphiphiles. However, in that case the chains in **Bn** compounds emanating from the corners of such polygons would have a problem reaching the centre of the cell. Even though geometrically possible, stretching of alkyl chains to maintain high density at the centre of pentagonal or even square cells at higher temperatures would be entropically disfavoured. Hence an alternative solution is adopted by the Y-shaped **An** molecules, abandoning the tangential in favour of axial alignment of the cores. There must, however, be a free energy penalty for this inversion, as in most other cases the tangential structure prevails. A possible penalty is the dilution of hydrogen bonding glycerol groups in (perforated) 2D layers in $P6/mmm$ and SmA+ phases, in contrast to their concentration in well segregated 1D columns in tangential honeycombs. Thus, as in many other examples, a relative minor alteration in molecular design leads to frustration resolved by the system adopting novel and potentially advantageous mesostructures.

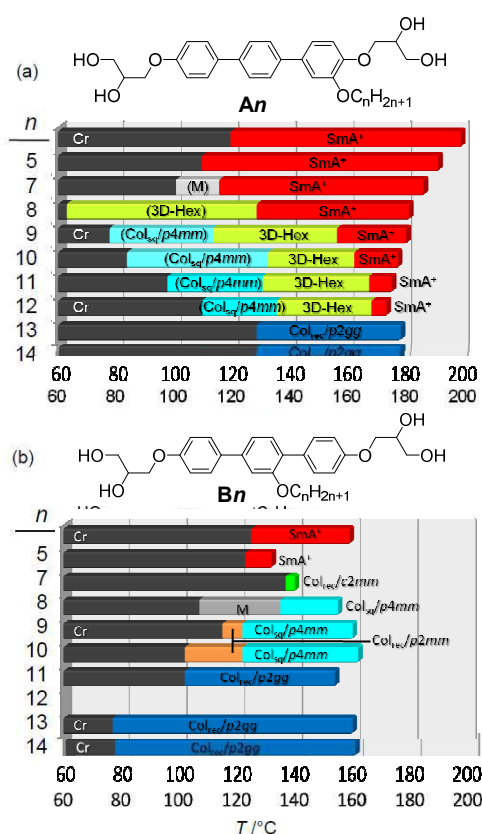


Figure 5. Comparison of the LC phases on cooling (10 K min^{-1}) a) of the Y-shaped (**An**) and b) the T-shaped bolopolyphiles **Bn**¹² depending on the length of the lateral chain n ; abbreviations: see Table 1 and 3D-Hex = $P6/mmm$; $\text{Col}_{\text{rec}}/c2mm$ = rhombic honeycomb; $\text{Col}_{\text{rec}}/p2mm$ = rectangular honeycomb; Col_{sq} = Col_{sq} in brackets were only observed on cooling.

A similar sequence $\text{SmA}^+ \rightarrow P6/mmm$ has been observed for facial amphiphiles with exchanged positions of alkyl chains and polar groups at the p -terphenyl core.¹³ In this $P6/mmm$ phase the polar lateral groups form the columns on the hexagonal lattice and the alkyl chains separate the layers of the coaxially aligned p -terphenyl rods (“channelled layer phase”, ChL_{hex}).¹³ In another related structure, the so-called “tubular nematic columnar phase”, formed by hairy-rod polymers¹⁷ and some oligomesogens,¹⁴ the mesogens are also co-axial to lipophilic columns, but have only orientational order. This indicates that co-axial honeycombs represent a general mode of LC self-assembly.

In summary, a new kind of LC honeycombs with co-axial rod orientation is reported, occurring at the transition from lamellar phases to tangential honeycombs and competing with the triangular and square honeycombs as well as with the bicontinuous cubic phases¹⁵. This work shows that an inversion of rod orientation in the honeycombs from tangential⁶ via tilted⁸ to co-axial provides a source of new complex LC phases, similar to the orthogonal (SmA), tilted (SmC)¹ and in-plane (Lam) versions of lamellar phases.¹⁶ From an application point of view the reported molecules represent simple generic model compounds for the understanding and tailoring of the self-assembly of larger π -conjugated molecules and lateral substituted rod-like macromolecules¹⁷ into well-defined superstructures, as required for advanced organic electronic and light harvesting applications.¹⁸

This work is supported by DFG (392435074), NSFC (21761132033, 21374086) and EPSRC (EP-P002250). We thank Beamlines BL16B1 at SSRF, I22 at Diamond Light Source and BM28 at ESRF for providing the beamtime.

There are no conflicts of interest to declare.

Notes and references

- ^a Department of Chemistry, Martin Luther University Halle-Wittenberg, Kurt-Mothes-Str. 2, 06120 Halle, Germany. E-mail: carsten.tschierske@chemie.uni-halle.de
- ^b State Key Laboratory for Mechanical Behavior of Materials, Xi'an Jiaotong University, Xi'an 710049, P. R. China. E-mail: feng.liu@xjtu.edu.cn
- ^c Department of Materials Science and Engineering, Sheffield University, Sheffield S1 3JD, UK. E-mail: g.ungar@sheffield.ac.uk
- † Electronic Supplementary Information (ESI) available: [Synthesis, analytical data, experimental techniques, DSC and XRD data, structural models and additional discussions]. See DOI: 10.1039/b000000x/
- 1 J. W. Goodby, P. J. Collings, T. Kato, C. Tschierske, H. F. Gleeson, P. Raynes, Eds.; *Handbook of Liquid Crystals*, 2nd Ed.; Wiley-VCH, Weinheim, Germany, 2014.
- 2 C. Tschierske, *Angew. Chem. Int. Ed.*, 2013, **52**, 8828; T. Kato, M. Yoshio, T. Ichikawa, B. Soberats, H. Ohno and M. Funahashi, *Nat. Rev. Mater.*, 2017, **2**, 17001; I. M. Saez, and J. W. Goodby, *J. Mater. Chem.* 2005, **15**, 26; W. Li, Y. Kim and M. Lee, *Nanoscale*, 2013, **5**, 7711.
- 3 S. Kumar, *Chemistry of Discotic Liquid Crystals*, CRC Press, Boca Raton, 2011; T. Wöhrle, I. Wurzbach, J. Kirres, A. Kostidou, N. Kapernaum, J. Litterscheidt, J. C. Haenle, P. Staffeld, A. Baro, F. Giesselmann and S. Laschat, *Chem. Rev.*, 2016, **116**, 1139.
- 4 H.-T. Nguyen, C. Destradre and J. Malthete, *Adv. Mater.*, 1997, **9**, 375.
- 5 X. H. Cheng, M. Prehm, M. K. Das, J. Kain, U. Baumeister, S. Diele, D. Leine, A. Blume and C. Tschierske, *J. Am. Chem. Soc.*, 2003, **125**, 10977.
- 6 a) C. Tschierske, *Chem. Soc. Rev.*, 2007, **36**, 1930; b) C. Tschierske, C. Nümberger, H. Ebert, B. Glettner, M. Prehm, F. Liu, X. B. Zeng and G. Ungar, *Interface Focus*, 2012, **2**, 669.
- 7 a) A. J. Crane, F. J. Martinez-Veracoechea, F. A. Escobedo and E. A. Muller, *Soft Matter*, 2008, **4**, 1820; (b) X. Liu, K. Yang and H. Guo, *J. Phys. Chem. B*, 2013, **117**, 9106.
- 8 M. Poppe, C. Chen, F. Liu, M. Prehm, S. Poppe, C. Tschierske, *Soft Matter*, 2017, **13**, 4676.
- 9 a) M. Prehm; F. Liu, X. Zeng, G. Ungar, and C. Tschierske, *J. Am. Chem. Soc.*, 2011, **133**, 4906; (b) F. Liu, M. Prehm, X. Zeng, C. Ungar and C. Tschierske, *Angew. Chem. Int. Ed.*, 2011, **50**, 10599.
- 10 M. Leaver, A. Fogden, M. Holmes and C. Fairhurst, *Langmuir*, 2001, **17**, 35.
- 11 N. K. Oh, W.-C. Zin, J.-H. Im and M. Lee, *Polymer*, 2006, **47**, 5375.
- 12 A. Lehmann, A. Scholte, M. Prehm, F. Liu, X.B. Zeng, G. Ungar and C. Tschierske, *Adv. Funct. Mater.*, 2018, DOI: 10.1002/adfm.201804162
- 13 a) B. Chen, X. B. Zeng, U. Baumeister, S. Diele, G. Ungar and C. Tschierske, *Angew. Chem. Int. Ed.* 2004, **43**, 4621; b) B. Chen, U. Baumeister, G. Pelzl, M. K. Das, X. B. Zeng, G. Ungar and C. Tschierske, *J. Am. Chem. Soc.*, 2005, **127**, 16578.
- 14 I. M. Saez, J. W. Goodby and R. M. Richardson, *Chem. Eur. J.*, 2001, **7**, 2758.
- 15 M. Poppe, C. Chen, H. Ebert, S. Poppe, M. Prehm, K. Kerzig, F. Liu, and C. Tschierske, *Soft Matter*, 2017, **13**, 4381; M. Poppe, C. Chen, F. Liu, S. Poppe and C. Tschierske, *Chem. Eur. J.*, 2017, **23**, 7196.
- 16 M. Prehm, X. H. Cheng, S. Diele, M. K. Das, C. Tschierske, *J. Am. Chem. Soc.*, 2002, **124**, 12072.
- 17 J. Watanabe, N. Sekine, T. Nematsu and M. Sone, *Macromolecules*, 1996, **29**, 4816.
- 18 T. Brixner, R. Hildner, J. Köhler, C. Lambert and F. Würthner, *Adv. Energy Mater.*, 2017, **7**, 1700236.

Supporting Information

Transition between tangential and co-axial liquid crystalline honeycombs in the self-assembly of Y-shaped bolapolyphiles

Anne Lehmann¹, Marko Prehm¹, Changlong Chen², Feng Liu^{2,*}, Xiangbing Zeng³, Goran Ungar^{3*}, Carsten Tschierske^{1,*}

¹ Department of Chemistry, Martin Luther University Halle-Wittenberg, Kurt-Mothes-Str. 2, 06120 Halle, Germany

² State Key Laboratory for Mechanical Behavior of Materials, Xi'an Jiaotong University, Xi'an 710049, P. R. China

³ Department of Materials Science and Engineering, Sheffield University, Sheffield S1 3JD, UK

1. Experimental techniques

1.1 XRD

X-ray scattering on aligned samples. - X-ray investigations were carried out at Cu K α line ($\lambda = 1.54 \text{ \AA}$) using a standard Coolidge tube source with a Ni-filter. Aligned samples were obtained on a glass plate on a temperature-controlled heating stage. Alignment was achieved upon slow cooling (rate: $1 \text{ K}\cdot\text{min}^{-1} - 0.01 \text{ K}\cdot\text{min}^{-1}$) of a small droplet of the sample and takes place at the sample–glass or at the sample–air interface. The aligned samples were held on a temperature-controlled heating stage and the diffraction patterns were recorded with a 2D detector (HI-STAR, Siemens); the exposure time was 15 min for WAXS and 30 min for SAXS. The distance between the sample and the detector was 9.0 cm (WAXS) or 26.8 cm (SAXS), and the beam was parallel to the substrate.

Synchrotron X-ray diffraction and electron density reconstruction.- High-resolution small-angle powder diffraction experiments were recorded on Beamline I22 at Diamond Light Source and Beamline BL16B1 at Shanghai Synchrotron Radiation Facility, SSRF. Samples were held in evacuated 1 mm capillaries. A modified Linkam hot stage with a thermal stability within $0.2 \text{ }^\circ\text{C}$ was used, with a hole for the capillary drilled through the silver heating block and mica windows attached to it on each side. A MarCCD detector was used. q calibration and linearization were verified using several orders of layer reflections from silver behemate and a series of n -alkanes. The measurement of the positions and intensities of the diffraction peaks is carried out using Galactic PeakSolveTM program, where experimental diffractograms are fitted using Gaussian shaped peaks. The diffraction peaks are indexed on the basis of their peak positions, and the lattice parameters and the space groups are subsequently determined. Once the diffraction intensities are measured and the corresponding space group determined, 3-d electron density maps can be reconstructed, on the basis of the general formula

$$E(xyz) = \sum_{hkl} F(hkl) \exp[i2\pi(hx+ky+lz)] \quad (\text{Eqn. 1})$$

Here $F(hkl)$ is the structure factor of a diffraction peak with index (hkl) . It is normally a complex number and the experimentally observed diffraction intensity

$$I(hkl) = K \cdot F(hkl) \cdot F^*(hkl) = K \cdot |F(hkl)|^2 \quad (\text{Eqn. 2})$$

Here K is a constant related to the sample volume, incident beam intensity etc. In this paper we are only interested in the relative electron densities, hence this constant is simply taken to be 1. Thus the electron density

$$E(xyz) = \sum_{hkl} \sqrt{I(hkl)} \exp[i2\pi(hx+ky+lz) + \phi_{hkl}] \quad (\text{Eqn. 3})$$

for 2D structures $I(hk)$ and Eqn. (4) were used:

$$E(xy) = \sum_{hk} \sqrt{I(hk)} \exp[i2\pi(hx+ky) + \phi_{hk}] \quad (\text{Eqn. 4})$$

As the observed diffraction intensity $I(hk)$ is only related to the amplitude of the structure factor $|F(hk)|$, the information about the phase of $F(hk)$, ϕ_{hk} , can not be determined directly from experiment. However, the problem is much simplified when the structure of the ordered phase is centrosymmetric, and hence the structure factor $F(hk)$ is always real and ϕ_{hk} is either 0 or π .

This makes it possible for a trial-and-error approach, where candidate electron density maps are reconstructed for all possible phase combinations, and the “correct” phase combination is then selected on the merit of the maps, helped by prior physical and chemical knowledge of

the system. This is especially useful for the study of nanostructures, where normally only a limited number of diffraction peaks are observed.

GISAXS experiments were carried out on station BM28 (XMaS line) at ESRF. Thin films were prepared from the melt on a silicon wafer. The thin film coated $5 \times 5 \text{ mm}^2$ Si plates were placed on top of a custom built heater, which was then mounted on a six-circle goniometer. A MarCCD 165 detector at ESRF was used. The sample enclosure and the beam pipe were flushed with helium.

1.2 POM and DSC

Polarizing Optical Microscopy (POM). Transition temperatures were measured using a Mettler FP-82 HT hot stage and control unit in conjunction with a Leica DMRXP polarizing microscope (Leica Microsystems GmbH, Wetzlar, Germany). Textures of the liquid crystalline mesophases were recorded with a Leica MC120 HD camera (Leica Microsystems GmbH, Wetzlar, Germany).

DSC measurements. DSC-thermograms were recorded on a DSC-7 (Perkin-Elmer GmbH & Co. KG, Überlingen, Germany) in $30 \mu\text{L}$ Al-pans with heating and cooling rates of $10 \text{ K}_{\text{min}}^{-1}$.

1.3 MD simulation

Annealing dynamics runs were carried out using the Universal Force Field (Material Studio, Accelrys). The structures in Fig. S20 were obtained with either 4 molecules in a square prism box or 20 molecules in a rectangular prism box and a height of 0.45 nm , with 3d periodic boundary conditions. 30 temperature cycles of NVT dynamics were run between 300 and 700 K , with a total annealing time of 30 ps .

2. Additional Data

2.1 DSCs and phase transitions

Table S1. Phase transition temperatures (DSC peak temperatures, 10 K min⁻¹) and corresponding transition enthalpy values [ΔH (kJ mol⁻¹)] of compounds **An** on heating (H) and cooling (C) ^a

An	Phase transitions
A5	H: Cr 167 [18.5] SmA+ 206 [6.2] Iso C: Iso 203 [6.7] SmA+ 114 [18.2] Cr
A7	H: Cr 156 [22.8] SmA+ 194 [6.4] Iso C: Iso 191 [6.6] SmA+ 105 [16.2] Cr
A8	H: Cr 156 [24.7] SmA+ 190 [5.8] Iso C: Iso 187 [6.0] SmA+ 116 [0.8] <i>P6/mmm</i> 101 [18.1] Cr
A9	H: Cr 145 [20.7] SmA+ 186 [4.9] Iso C: Iso 182 [5.2] SmA+ 130 [0.8] <i>P6/mmm</i> 95 [-] M 65 [2.4] ^b Cr
A10	H: Cr 150 [26.8] (<i>Col_{squ}/p4mm</i> 124 [1.8]) <i>P6/mmm</i> 159 [0.9] SmA+ 184 [4.5] Iso C: Iso 182 [4.7] SmA+ 157 [1.0] <i>P6/mmm</i> 115 [1.8] <i>Col_{squ}/p4mm</i> 78 [11.3] Cr
A11	H: Cr 151 [24.0] (<i>Col_{squ}/p4mm</i> 140 [2.6]) <i>P6/mmm</i> 168 [1.0] SmA+ 181 [4.0] Iso C: Iso 179 [4.0] SmA+ 164 [1.2] <i>P6/mmm</i> 136 [2.4] <i>Col_{squ}/p4mm</i> 84 [13.4] Cr
A12	H: Cr 152 [26.8] (<i>Col_{squ}/p4mm</i> 137 [2.0]) <i>P6/mmm</i> 170 [1.4] SmA+ 179 [3.5] Iso C: Iso 178 [3.5] SmA+ 169 [1.4] <i>P6/mmm</i> 131 [2.3] <i>Col_{squ}/p4mm</i> 98 [17.1] Cr
A13	H: Cr 158 [27.5] (<i>Col_{squ}/p4mm</i> 140 [2.8]) <i>P6/mmm</i> 174 [1.6] SmA+ 177 [2.9] Iso C: Iso 177 [3.0] SmA+ 172 [1.7] <i>P6/mmm</i> 141 [3.2] <i>Col_{squ}/p4mm</i> 107 [18.4] Cr
A14	H: Cr 159 [29.7] <i>Col_{rec}/p2gg</i> 182 [6.5] Iso C: Iso 179 [6.2] <i>Col_{rec}/p2gg</i> 129 [26.0] Cr

^a H = heating, C = cooling; additional values in brackets were taken from the second heating scan; M = unknown mesophase; ^b only partial crystallisation.

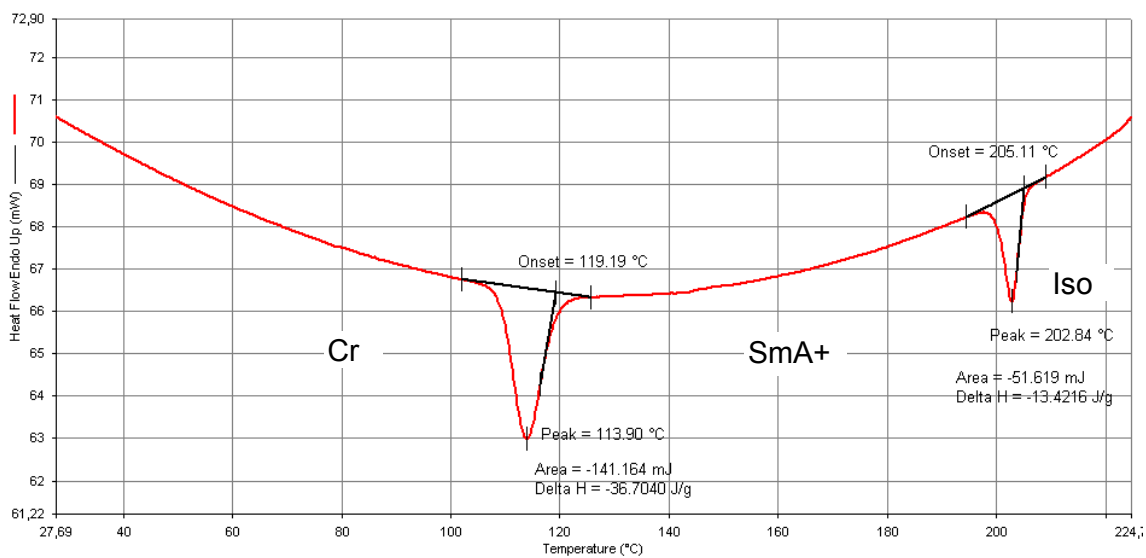
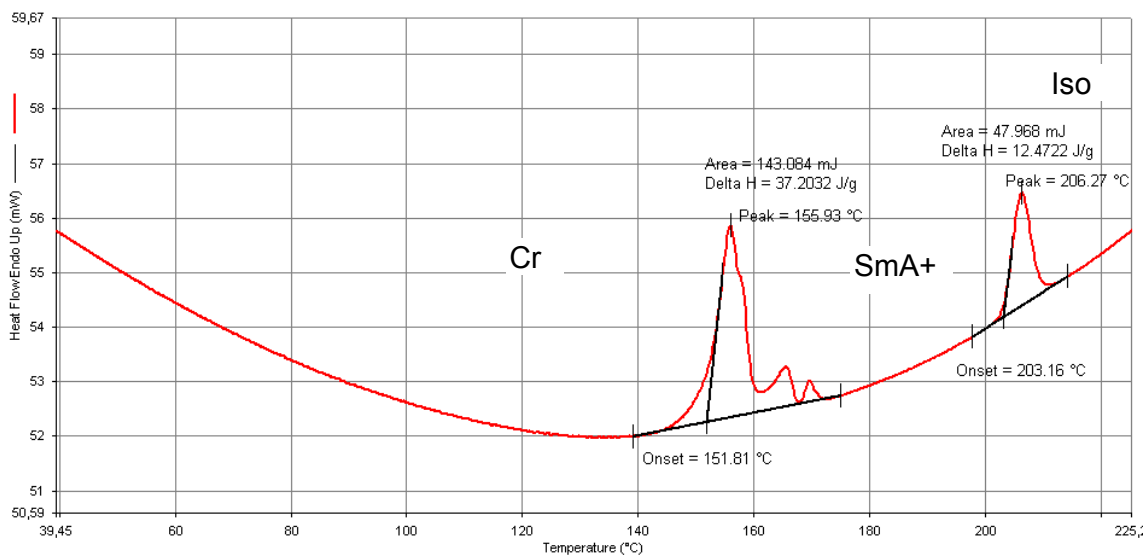


Figure S1a. Second DSC heating (top) and cooling scans (bottom) of compound **A5** at 10 K min⁻¹.

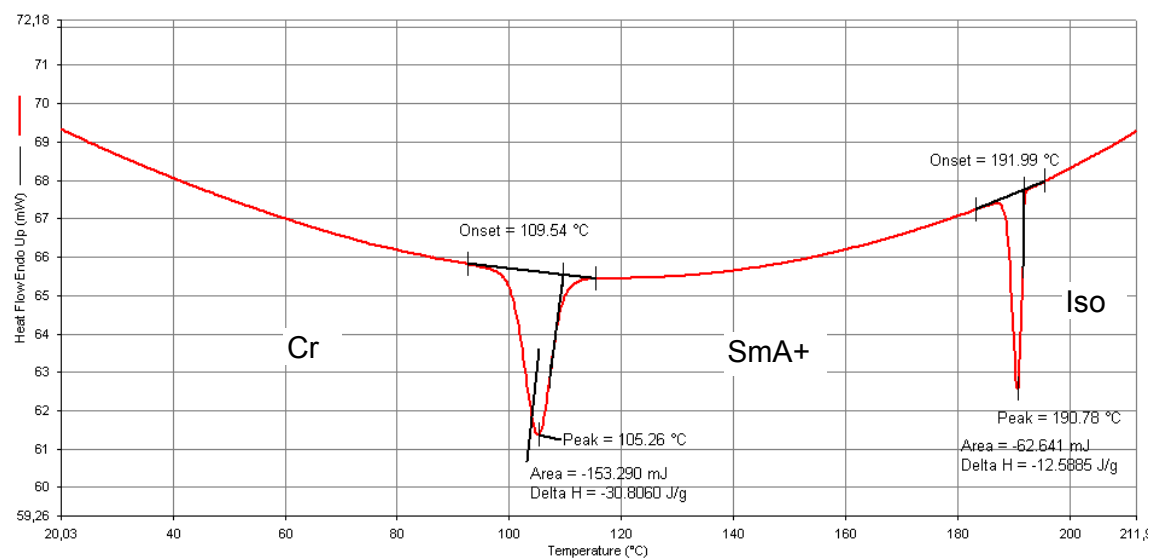
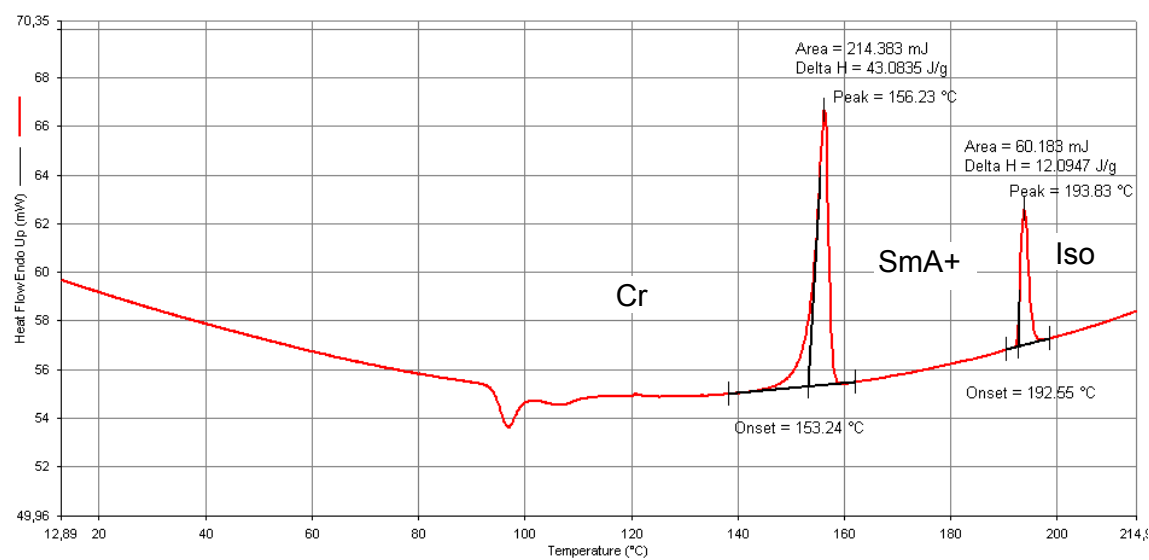


Figure S1b. First DSC heating (top) and cooling scans (bottom) of compound A7 at 10 K min⁻¹.

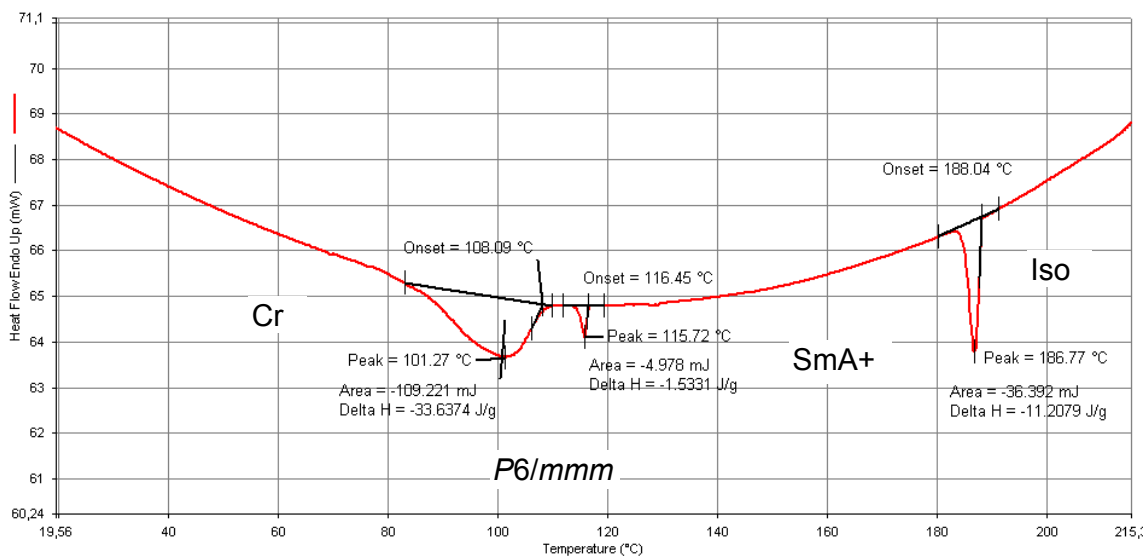
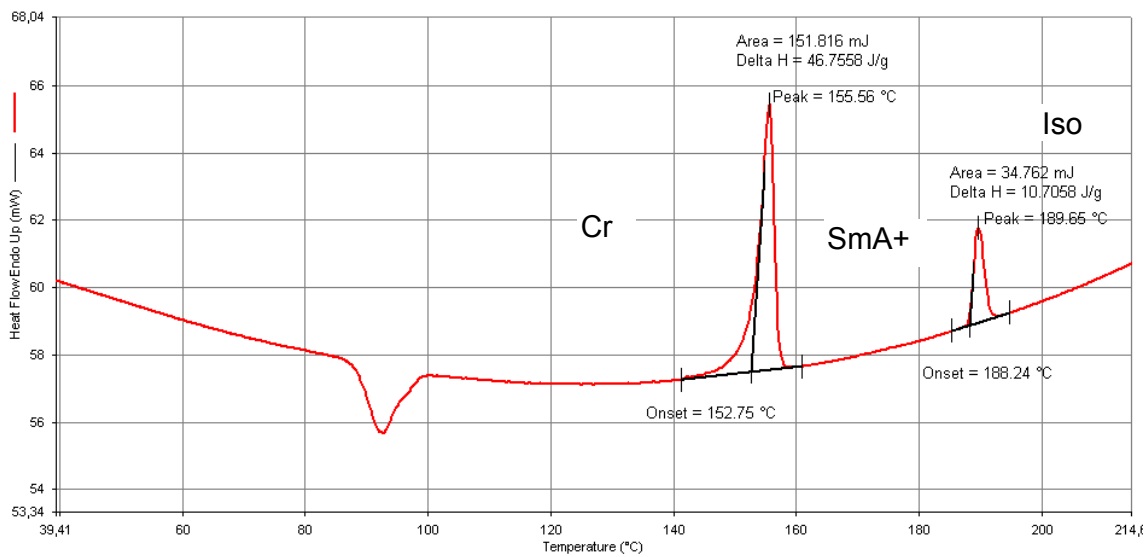


Figure S1c. First DSC heating (top) and cooling scans (bottom) of compound **A8** at 10 K min^{-1} .

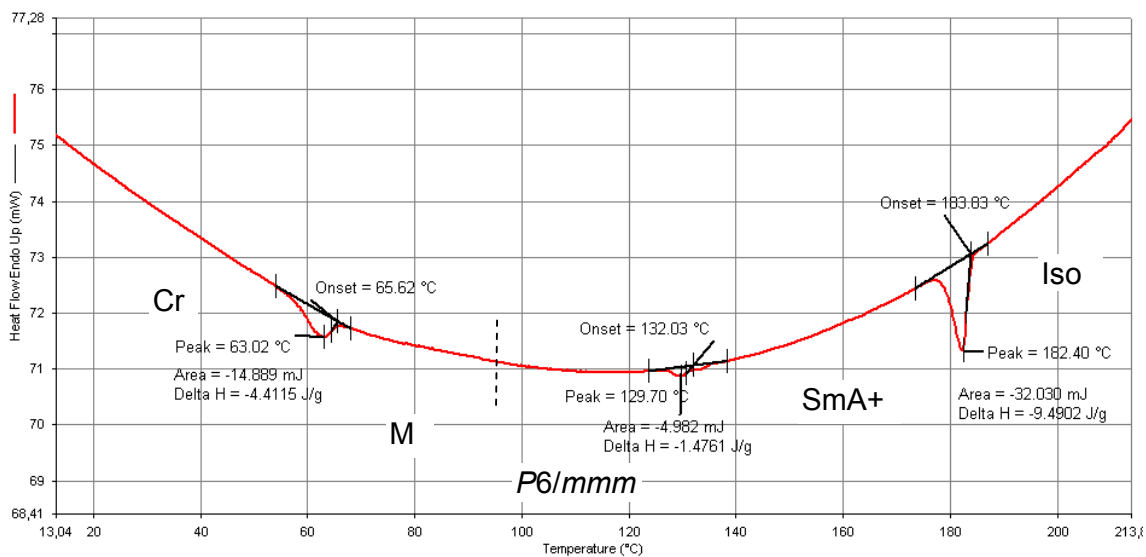
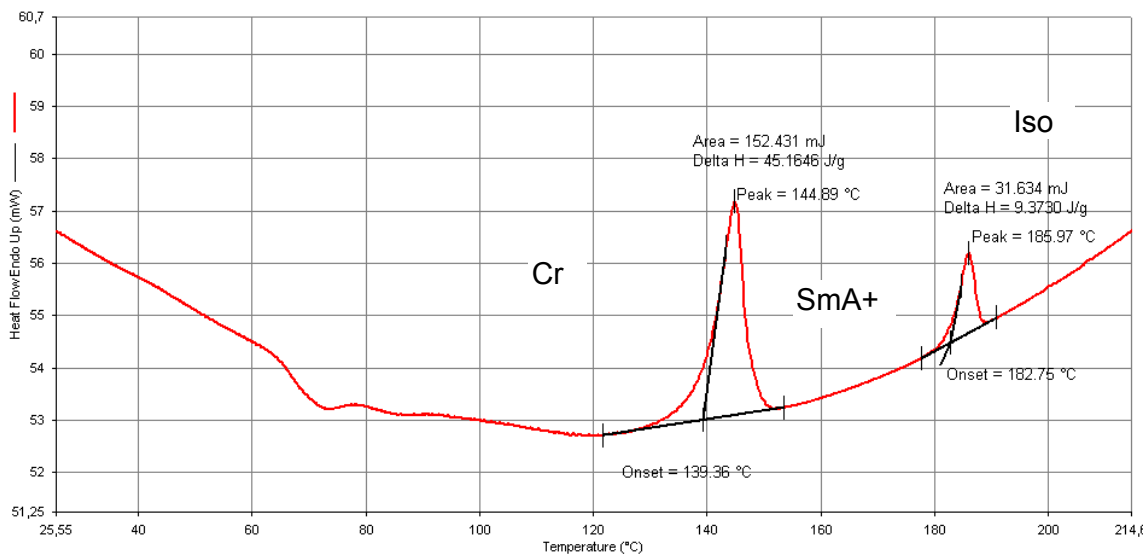


Figure S1d. First DSC heating (top) and cooling scans (bottom) of compound **A9** at 10 K min^{-1} .

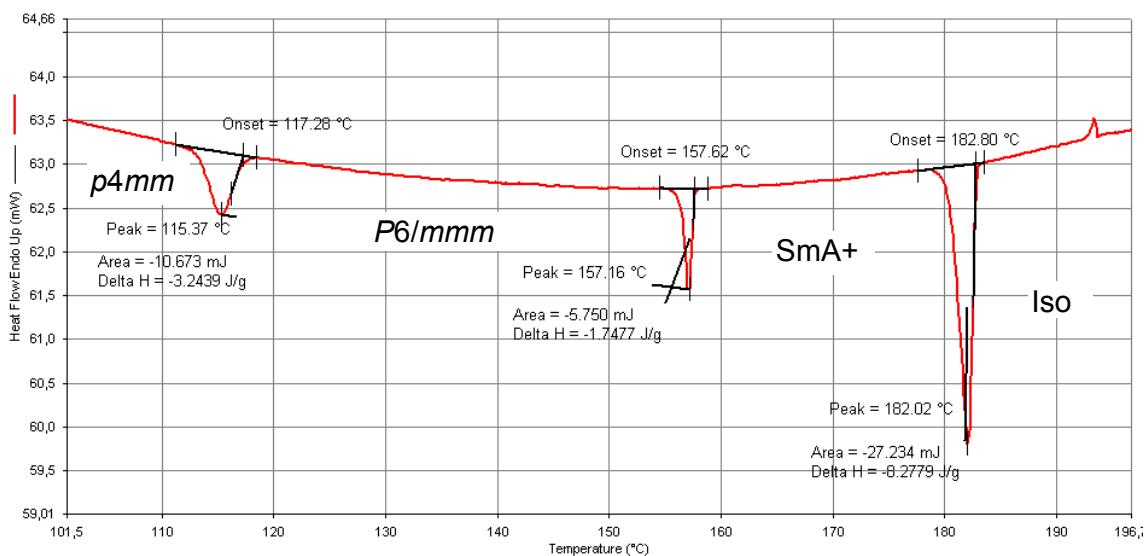
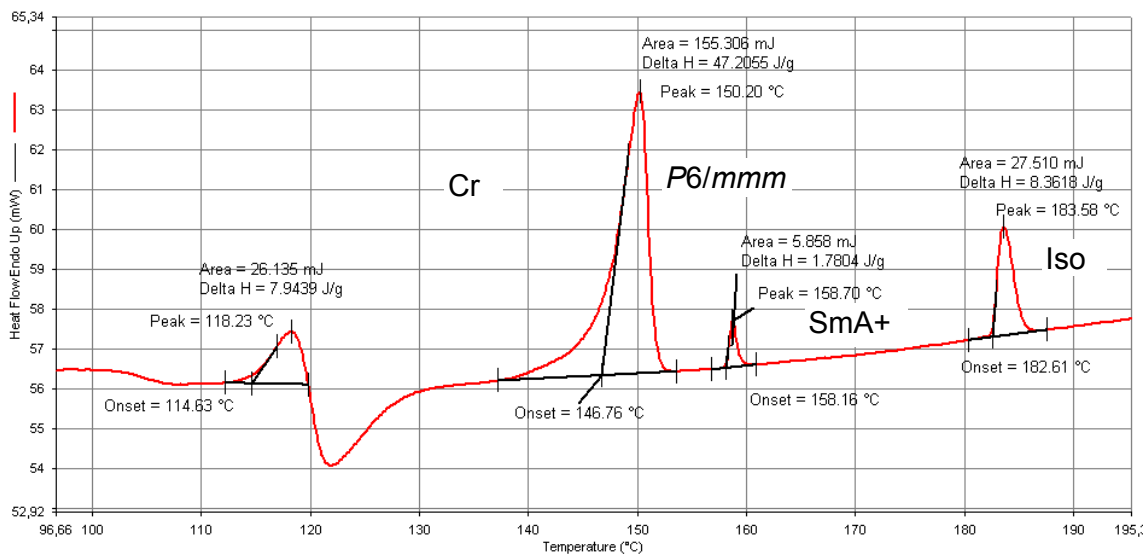


Figure S1e. First DSC heating (top) and cooling scans (bottom) of compound **A10** at 10 K min⁻¹.

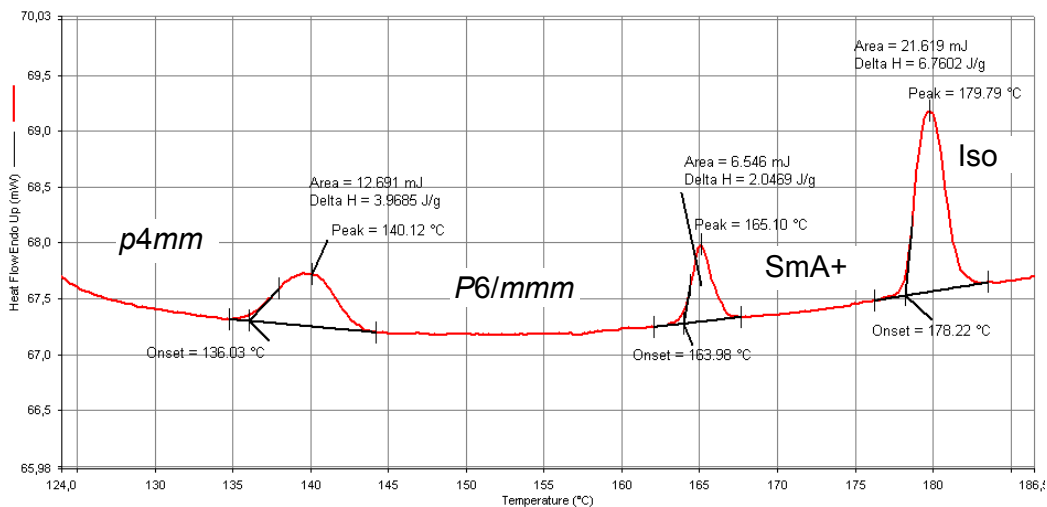
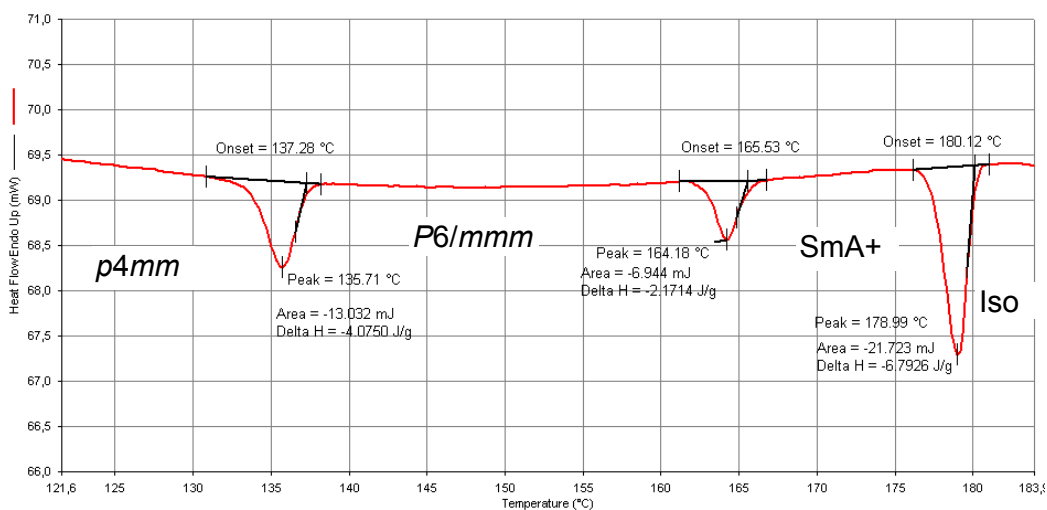
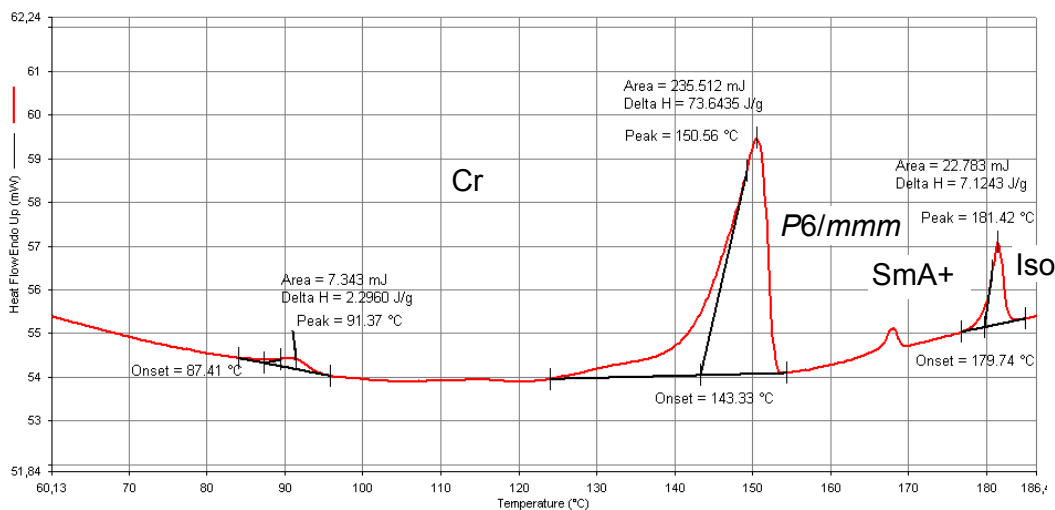


Figure S1f. DSC first heating (top), first cooling (middle) and second heating scans of compound A11 at 10 K min⁻¹.

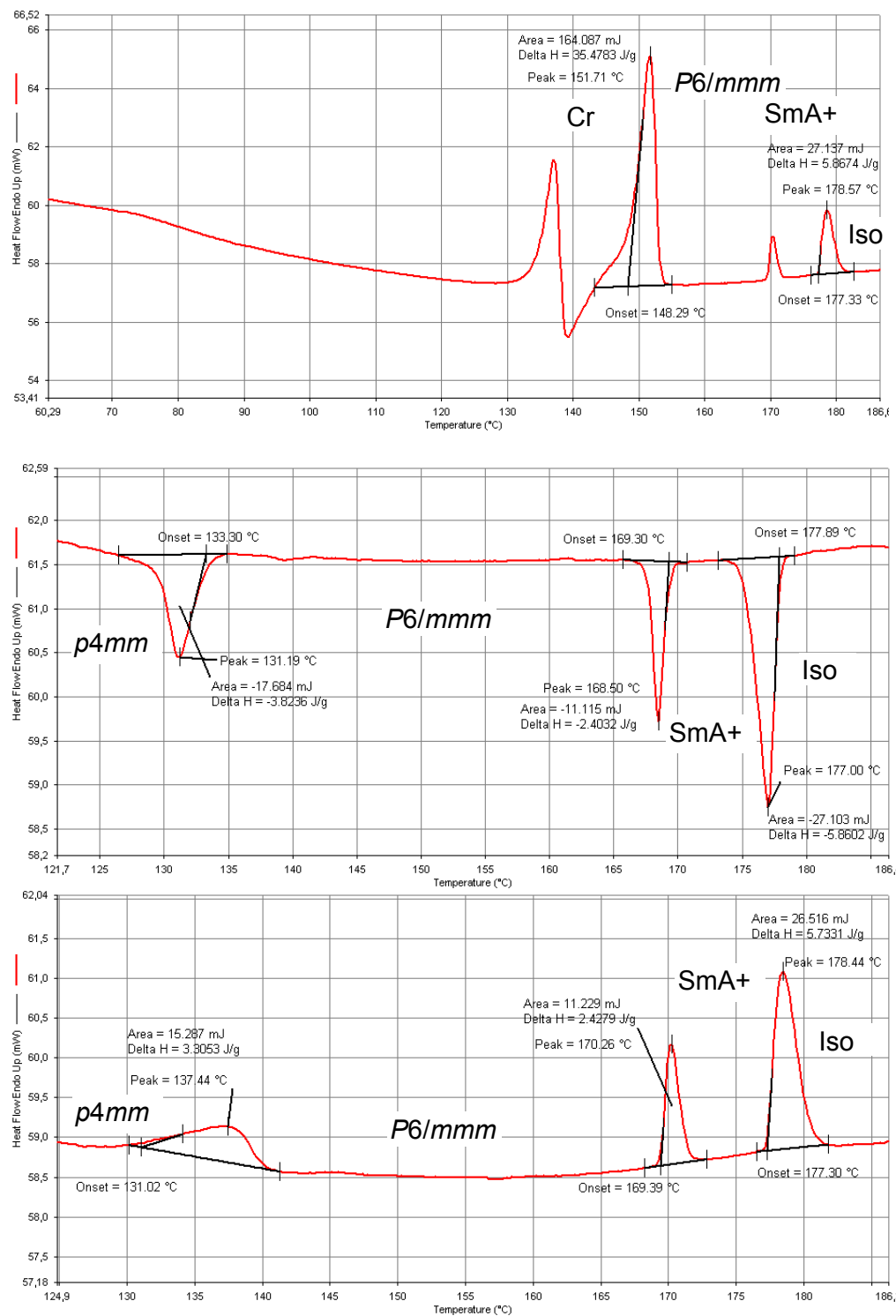


Figure S1g. DSC first heating (top), first cooling (middle) and second heating scans of compound A12 at 10 K min⁻¹.

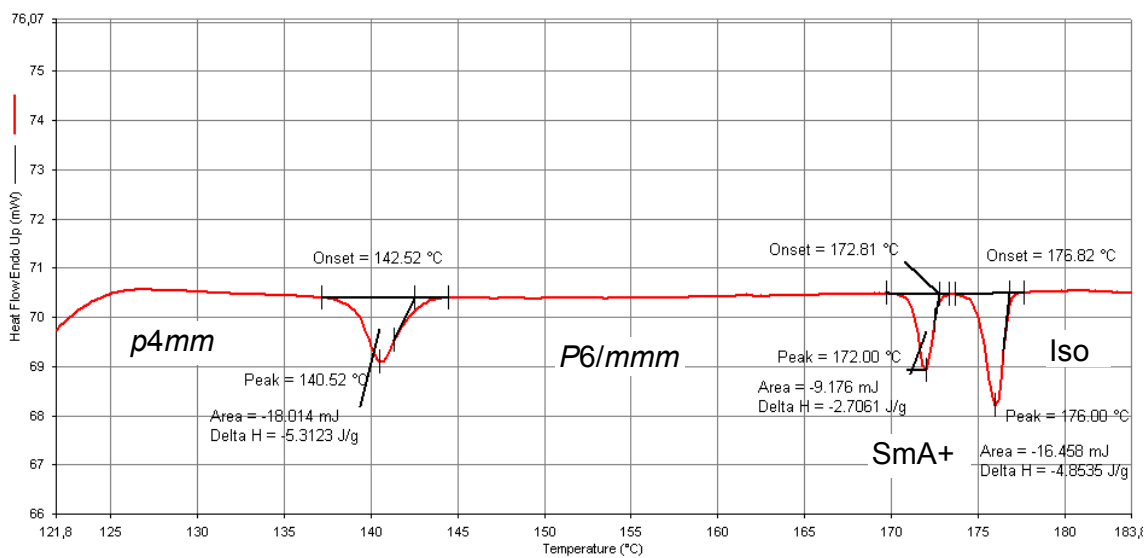
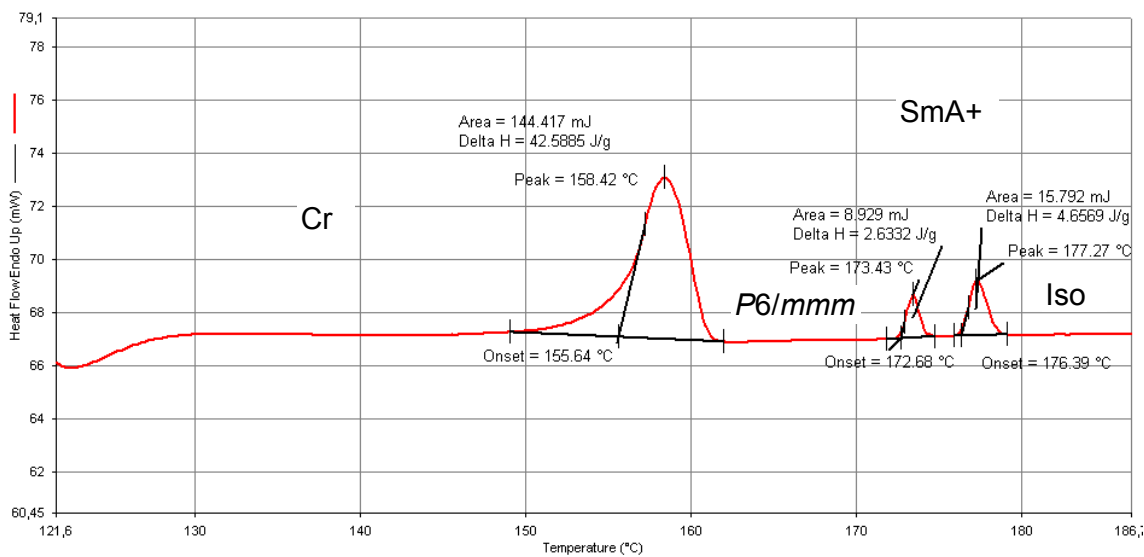


Figure S1h. Second DSC heating (top) and cooling scans (bottom) of compound **A13** at 10 K min^{-1} .

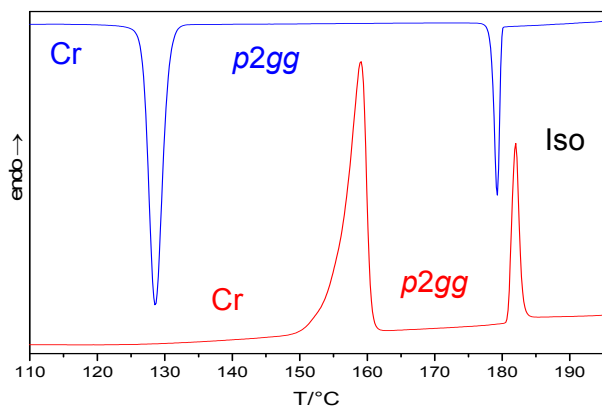


Figure S1i. First DSC heating (red) and cooling scans (blue) of compound **A14** at 10 K min^{-1} .

2.2 Additional textures

2.2.1 Compound A11

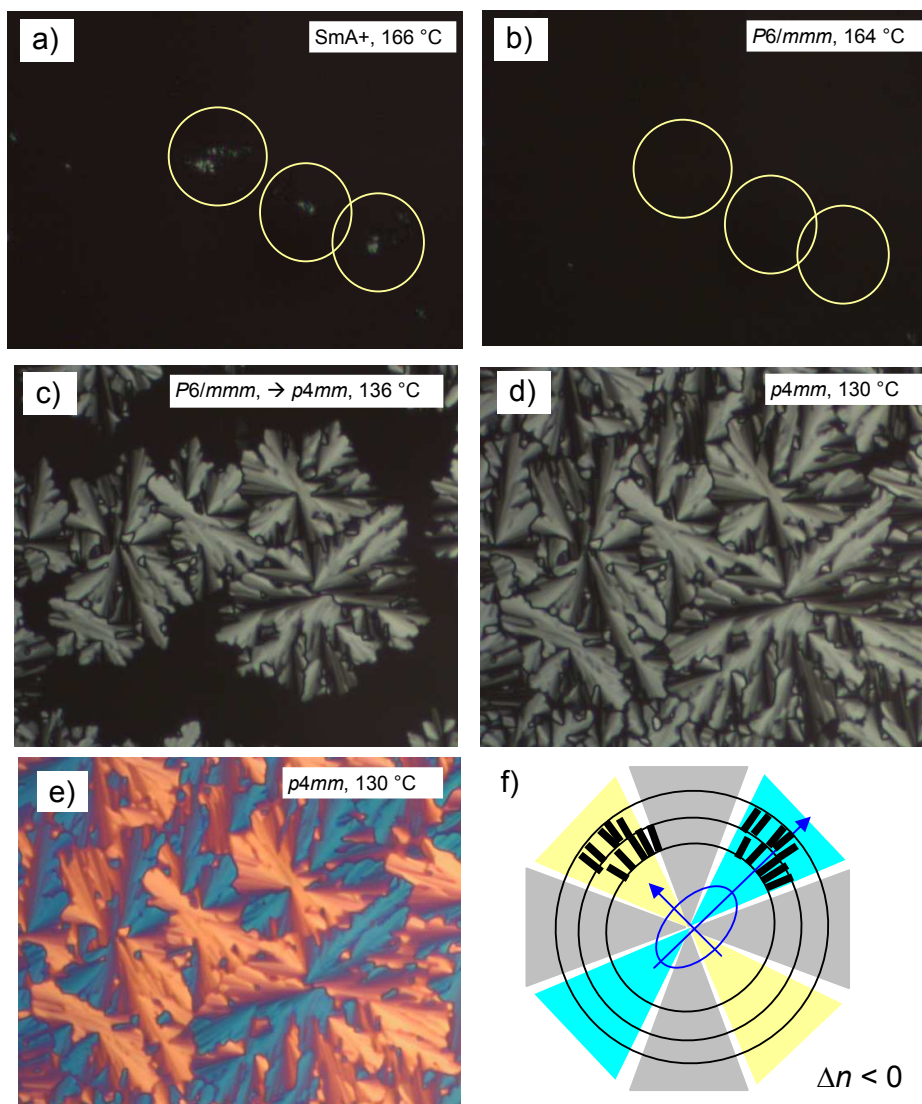


Figure S2. Phase transitions observed in a homeotropic sample surfaces (terphenyls perpendicular and the layer planes parallel to the surface) of **A11**. a) The homeotropic aligned SmA+ phase appears dark with some defects; b) the birefringent defects have disappeared after transition to $P6/mmm$; c) the transition to the $p4mm$ phase is associated with the development of a weakly birefringent spherulitic texture; d) shows the fully developed $p4mm$ phase. The development of birefringence indicates that the evolving $p4mm$ lattice has a different direction with respect to the previous hexagonal lattice in $P6/mmm$. Hence, the $p4mm$ lattice develops perpendicular to the hexagonal lattice, i.e. the lipophilic columns become organized parallel to the surfaces at the $P6/mmm - p4mm$ transition. Around the lipophilic columns the terphenyls are tangentially aligned and form square cylinders with the vertices (the columns of the hydrogen bonding glycerols) being pinned to the surface (edge-on-surface, see Fig. S3b). This provides an anticlinic 90° tilt between the p-terphenyls, explaining the relatively low birefringence of the homeotropic texture in d). e) Texture of the $Col_{squ}/p4mm$ phase with $\lambda/2$ -retarder plate and f) model showing the organization of the p-

terphenyl rods with respect to the indicatrix of the $\lambda/2$ plate. The high index axis of the $\lambda/2$ plate is 45° SW to NE. The soft square honeycombs form circles with a defect in the center. The blue shift in the direction of the high index axis of the retarder plate indicates negative birefringence, i.e. the orientation of the π -conjugated rods is perpendicular to the long axes of the prismatic cells, thus confirming a tangential-rod-honeycomb LC structure of the $p4mm$ phases.

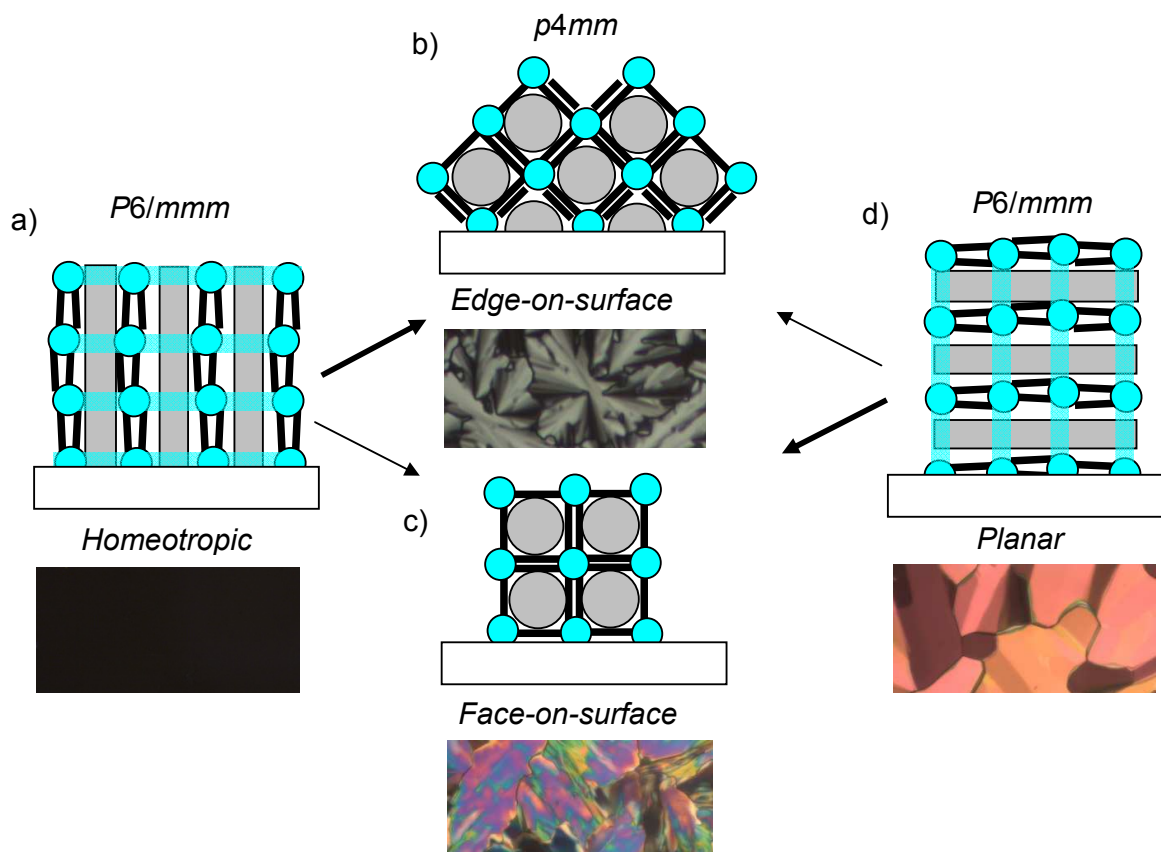


Figure S3. Models showing the alignment of compounds **An** in the three LC phases depending in the mode of alignment and the molecular reorganization at the phase transitions: a) Alignment of the molecules in the homeotropic sample of the $P6/mmm$ phase of **A11** and b,c) distinct modes of alignment in the $p4mm$ phase developing on cooling, b) edge-on-surface and c) face-on-surface. d) Alignment of the molecules in a planar sample of the $P6/mmm$ phase. The higher birefringence of the $p4mm$ phase obtained in the planar samples d) compared to the homeotropic samples a) suggests that in the first case the formation of the face-on-surface alignment c) and in the second case the edge-on-surface organization b) is preferably formed. Both modes of alignment can be observed in the GISAXS experiments (see Fig. S11c, red lattice = face-on arrangement and yellow lattice = edge-on arrangement). In the homeotropic alignment a) all rods are perpendicular to the surface and therefore $\Delta n = 0$ if viewed perpendicular to the surface. In the highly birefringent texture of the planar aligned $P6/mmm$ phase in d) the aromatics are parallel to the surface and therefore Δn has maximum value. In this alignment the transition from $P6/mmm$ to the $p4mm$ square honeycomb leads to a reduction of the birefringence (orange via green to blue in c)), because half of the molecules become aligned perpendicular to the surface, and these molecules do not significantly contribute to the observed birefringence. For arrangement c) the birefringence is higher than in b) because half of the molecules retain their organization parallel to the surfaces, whereas

in b) the organization of the π -conjugated rods is anticlinic with 90° angles, which is known to lead to a very small birefringence.^{S1}

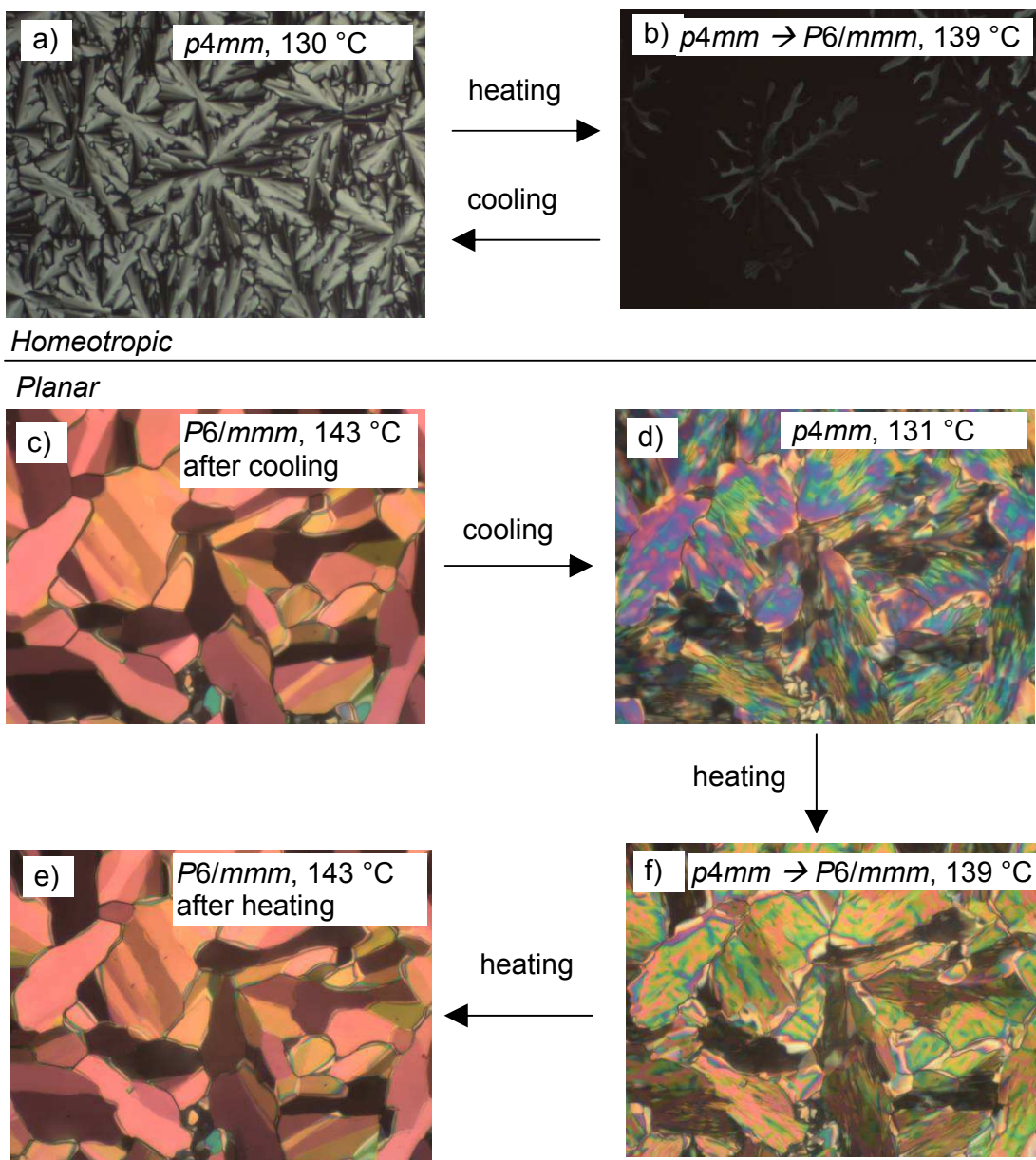


Figure S4. Reversibility of the $P6/mmm - p4mm$ phase transition of compound **A11** a,b) in homeotropic alignment and c-f) in planar alignment. The $P6/mmm - p4mm$ phase transitions are fully reversible, i.e. there is no temperature hysteresis (see DSCs in Fig. S1f-h) and for both modes of alignment the same textures as observed before the phase transition on cooling were reproducibly restored upon heating.

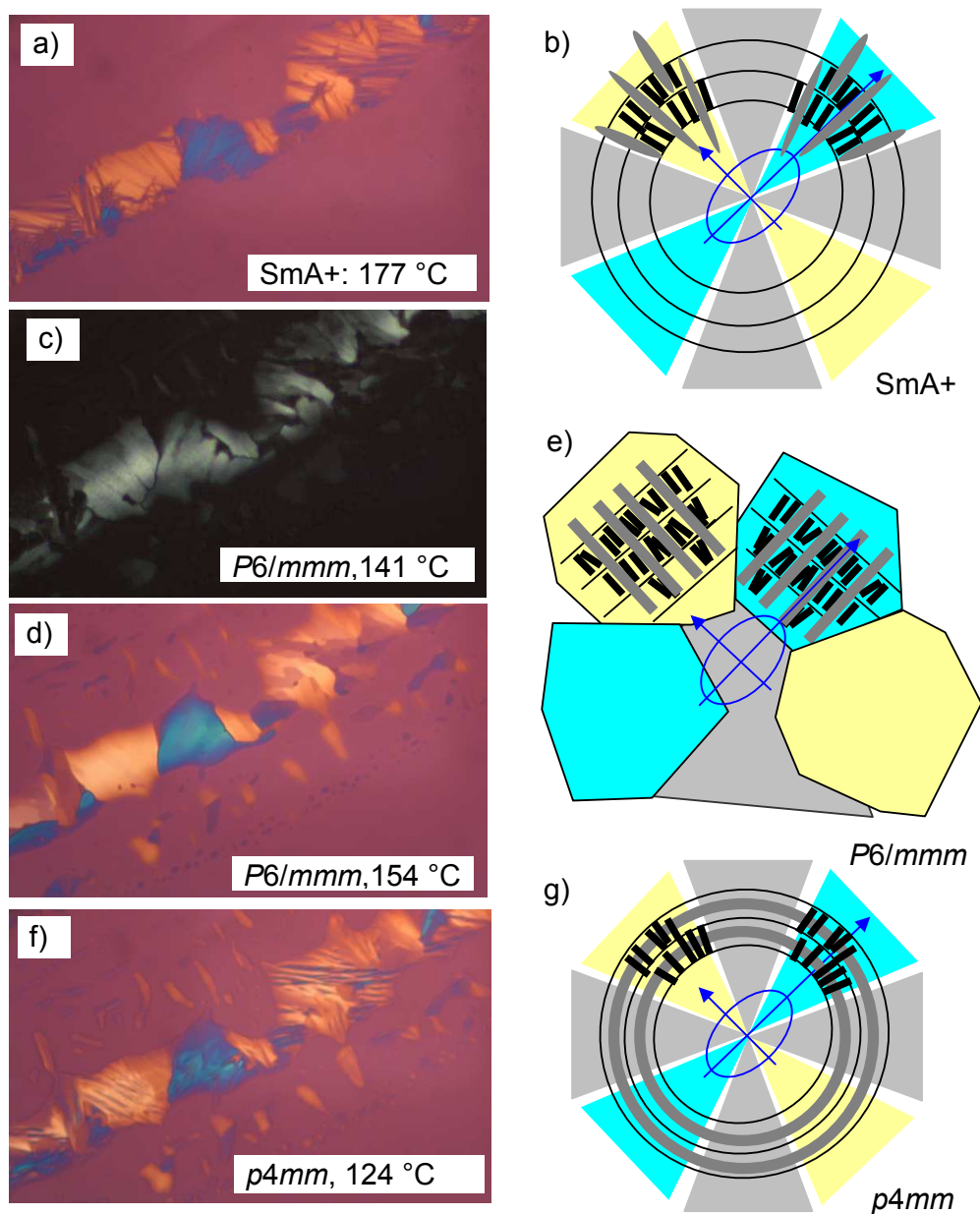


Figure S5. a,c,d,f) Textures observed for a non-covered thin film of **A11** in planar alignment (see also the insets in Fig. 2a-c) and b,e,g) models of azimuthal molecular organization (top view on the surface with indicatrix orientation and color shift of the differently aligned regions); a,b) soft layers of the SmA+ phase; c-e) rigid mosaic-like domains of the $P6/mmm$ phase and f,g) soft columns in the $p4mm$ phase. The indicatrix orientation of the $\lambda/2$ plate is shown in blue; the dark gray lines/circles indicate the columns of the lateral alkyl chains. The majority of blue shifted areas remain blue shifted and the yellow shifted remain yellow shifted during all three phase transition. This means that in planar alignment the azimuthal orientation of the aromatic cores, i.e. the direction of the terphenyls, does not change during the two phase transitions. This means that at the $P6/mmm$ - $p4mm$ phase transition the alkyl chain columns change their direction by 90° , which requires a disruption of these columns, followed by rebuilding in the perpendicular direction (e \rightarrow g).

2.2.2 Compound A14

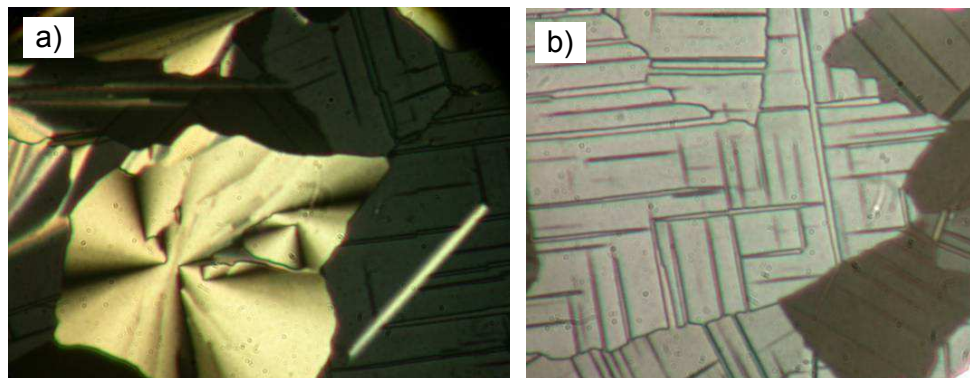


Figure S6. Textures of the $p2gg$ phase of **A14** at $T = 160$ °C showing the spherulitic texture (planar aligned regions) and the mosaic texture with stripe pattern in the homeotropic aligned sample.

2.3 Additional XRD data

2.3.1 Compound A5

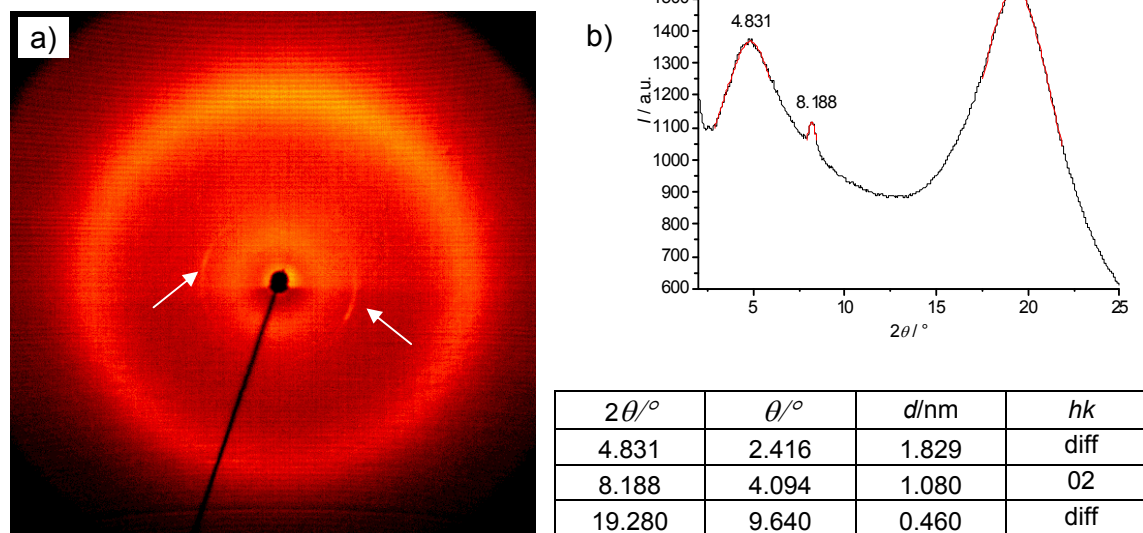


Figure S7. 2D-XRD pattern of an aligned sample of the SmA+ phase of **A5** at $T = 170$ °C. a) original pattern and b) θ -scan over this pattern with numerical data. The diffuse scattering in the small angle range ($d = 1.83$ nm) has an almost isotropic distribution, whereas the maximum of the diffuse wide angle scattering ($d = 0.46$ nm) has its maximum perpendicular to the direction of the layer reflection (arrows, 02) reflection, (01)-reflection is not visible; $d = 2.16$ nm). This indicates a strongly distorted layer structure with short range order between the domains involving the alkyl chains. These domains are small and apparently do not form columns penetrating the layers. The uniform distribution of the diffuse small angle scattering suggests the presence of small almost spherical domains.

2.3.2 Compound A8

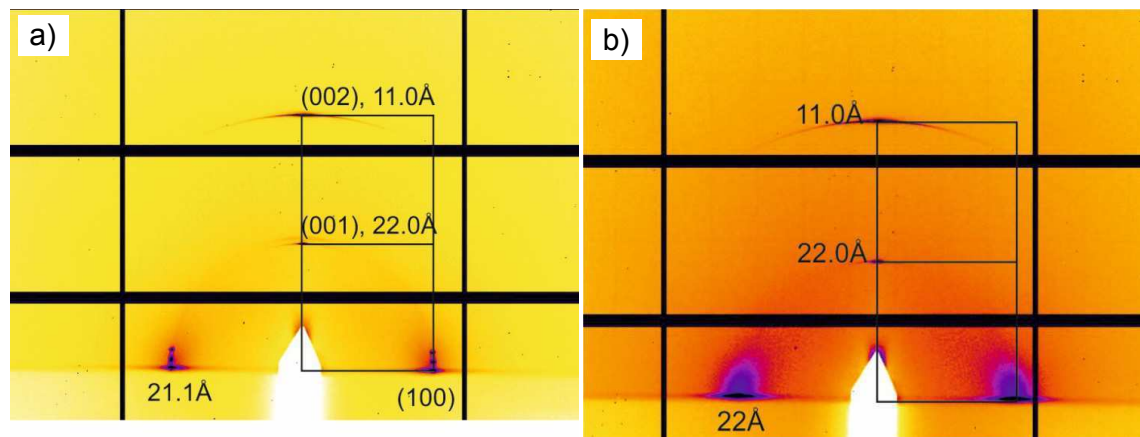


Figure S8. GISAXS patterns of compound **A8** a) in the $P6/mmm$ phase at 110 °C and b) in the SmA^+ phase at 130 °C, showing the diffuse scattering on the equator in b) coalescing to the bragg peaks in a).

2.3.3 Compound A9

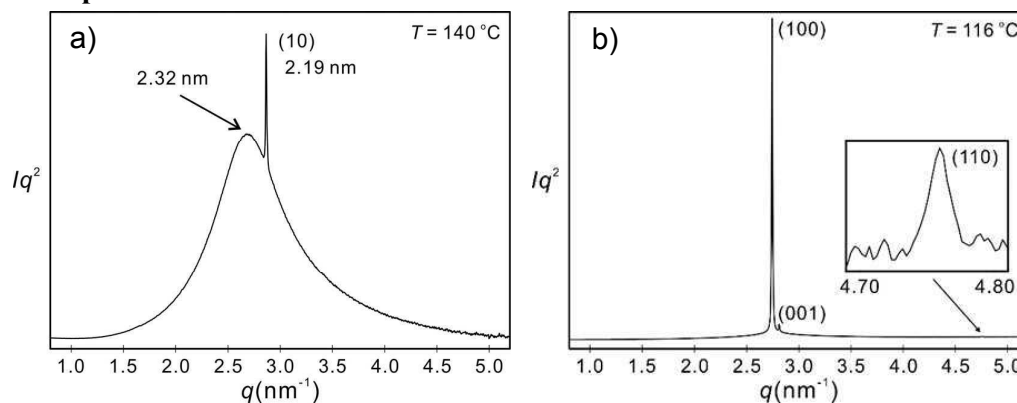


Figure S9. SAXS diffractogram of **A9**: (a) SmA^+ phase at 140 °C; (b) the $P6/mmm$ phase at 116 °C.

Table S2. Experimental and calculated d -spacings and relative integrated intensities, for the SmA^+ phase of **A9** at 140 °C and the $P6/mmm$ phase at 116 °C. All intensities values are Lorentz and multiplicity corrected.

(hk)	$d_{obs.}$ - spacings (nm)	$d_{cal.}$ - spacings (nm)	Intensity	Phase
(10)	2.19	2.19	100.0	/
	2.32			
$d = 2.18 \text{ nm}, d_2 = 2.32 \text{ nm}$				
(100)	2.29	2.29	100	0
(001)	2.23	2.23	4.7	0
(110)	1.32	1.32	0.2	0
$a = 2.64 \text{ nm}, c = 2.23 \text{ nm}$				

2.3.4 Compound A10

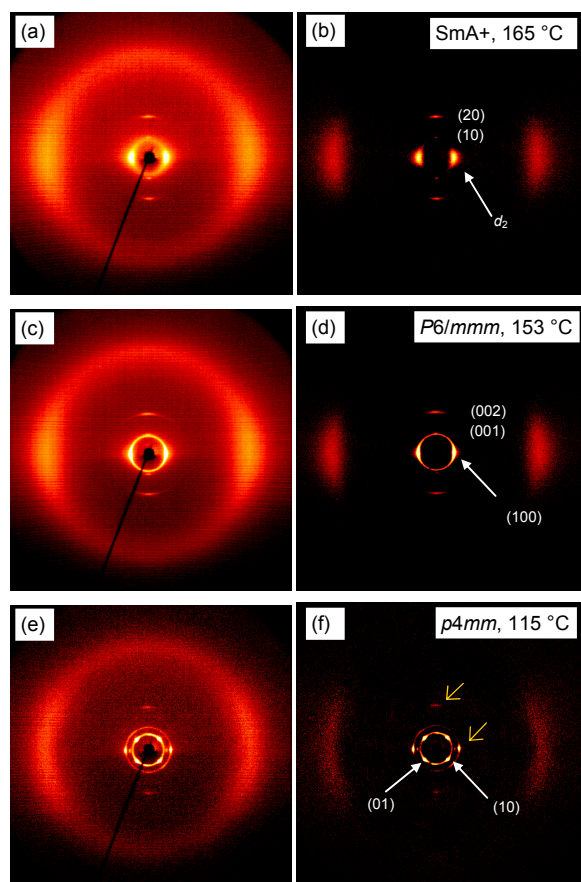


Figure S10. a-f) XRD patterns of an aligned sample of compound **A10** in the distinct LC phases at the indicated temperatures; a,c,e) are the original diffraction patterns; b,d,f) were obtained after subtraction of the scattering pattern in the isotropic liquid state; the yellow arrows in f) indicate the residual diffraction peaks from the *P6/mmm* phase.

Table S3. Numerical XRD data of the LC phases of compound **A10** (for diffraction patterns, see Figs. 3 and S10).

a) SmA^+ phase at $T = 165\text{ °C}$ ($d = 2.13\text{ nm}$)

$2\theta/\text{°}$	$\theta/\text{°}$	d/nm	hk
3.519	1.760	2.511	diff
4.148	2.074	2.130	10
8.215	4.108	1.076	20
19.431	9.716	0.457	diff

b) *P6/mmm* phase at $T = 153\text{ °C}$ ($a_{\text{hex}} = 2.84\text{ nm}$; $c = 2.17\text{ nm}$)

$2\theta/\text{°}$	$\theta/\text{°}$	d_{obs}/nm	hk	$d_{\text{calc}}/\text{nm}$	$d_{\text{obs}} - d_{\text{calc}}$
3.586	1.793	2.464	100	2.460	0.00
4.068	2.034	2.172	001	2.170	0.00
8.049	4.025	1.098	002	1.085	0.01
19.590	9.7925	0.453	diff	-	-

c) $p4mm$ phase at $T = 115\text{ }^\circ\text{C}$ ($a_{\text{squ}} = 2.81\text{ nm}$)

$2\theta/^\circ$	$\theta/^\circ$	d_{obs}/nm	hk	$d_{\text{calc}}/\text{nm}$	$d_{\text{obs}}-d_{\text{calc}}$
3.146	1.573	2.808	10	2.808	0.00
4.543	2.272	1.945	11	1.9857	0.04
19.679	9.840	0.451	diff	-	-

2.3.5 Compound A11

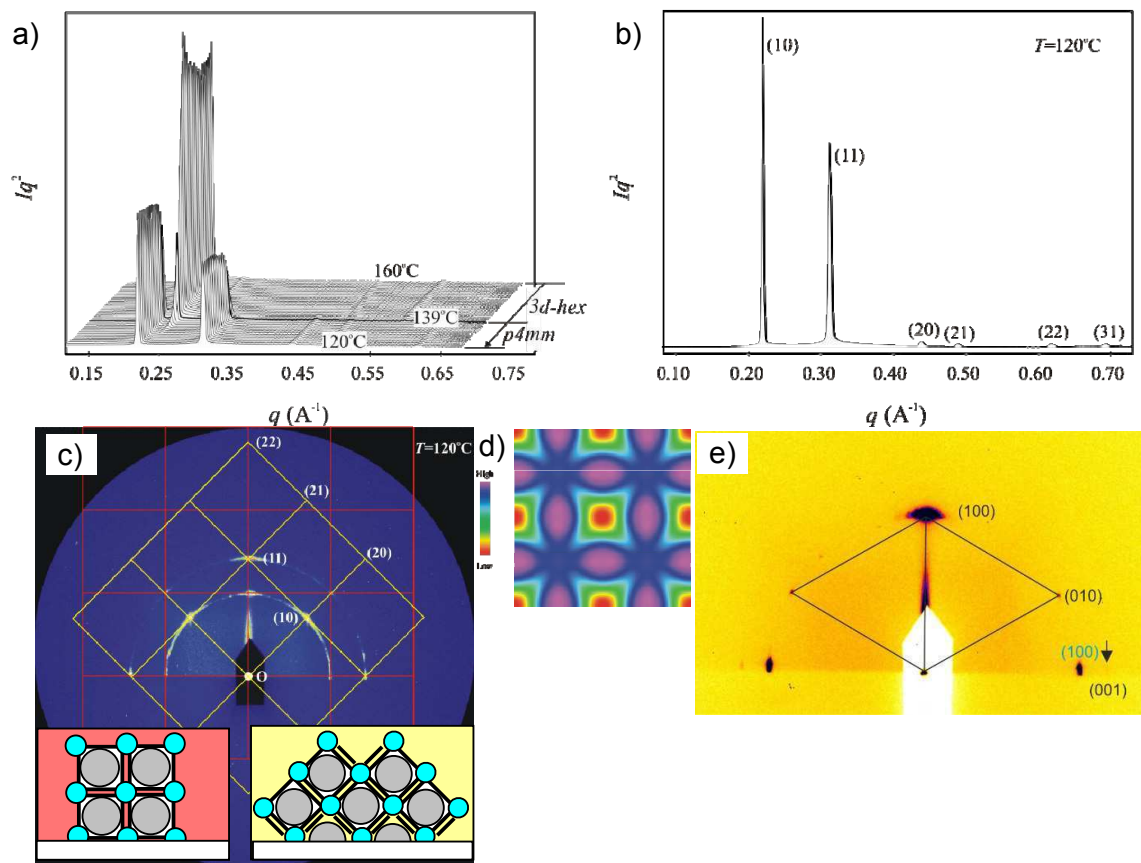


Figure S11. a) Powder pattern showing the temperature dependent development of the small angle scattering pattern of **A11**, b) diffraction pattern in the $p4mm$ phase at $120\text{ }^\circ\text{C}$, c) GISAXS pattern of the $p4mm$ phase on a Si surface at $120\text{ }^\circ\text{C}$; the insets show the two distinct modes of alignment (see also Fig. S3b); d) reconstructed electron density map of the the $p4mm$ phase (from data in Table S4) and e) GISAXS pattern of the $P6/mmm$ phase at $150\text{ }^\circ\text{C}$.

Table S4. Experimental and calculated d -spacings of the observed SAXS reflections of the square phase $p4mm$ in compound **A11** at 120 °C. All intensities values are Lorentz corrected with correction for multiplicity.

(hk)	$d_{\text{obs.}}$ -spacing (nm)	$d_{\text{cal.}}$ -spacing (nm)	$intensity$	$phase$
(10)	2.86	2.86	100.0	π
(11)	2.01	2.02	87.6	π
(20)	1.43	1.43	2.5	π
(21)	1.28	1.28	0.8	π
(22)	1.02	1.01	1.6	0
(31)	0.91	0.90	0.5	0
$a_{\text{squ}} = 2.86 \text{ nm}$				

2.3.6 Compound A12

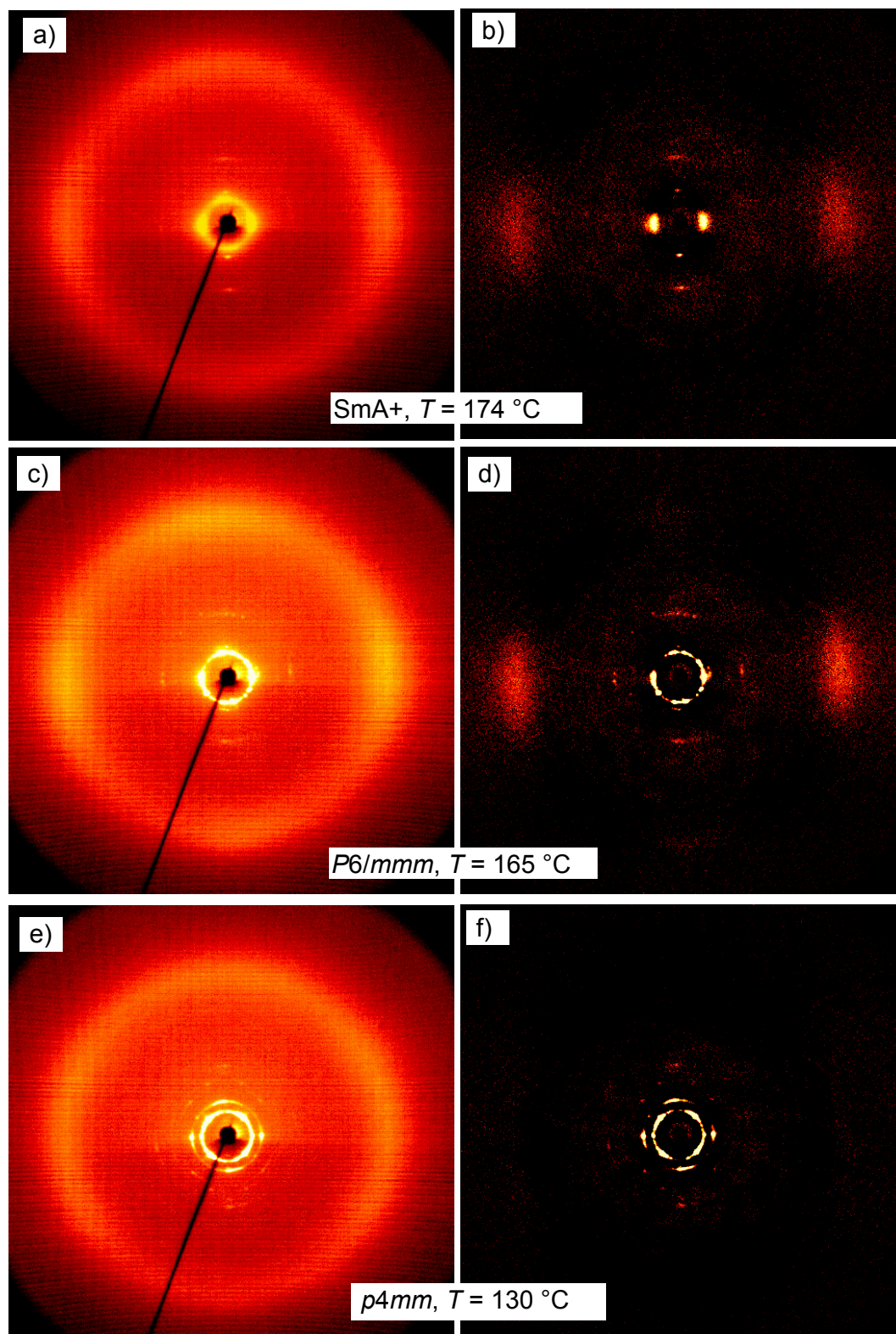


Figure S12. 2D XRD patterns of an aligned sample of compound A12 in the distinct LC phases at the indicated temperatures; a,c,e) are the original diffraction patterns; b,d,f) were obtained after subtraction of the scattering pattern in the isotropic liquid state.

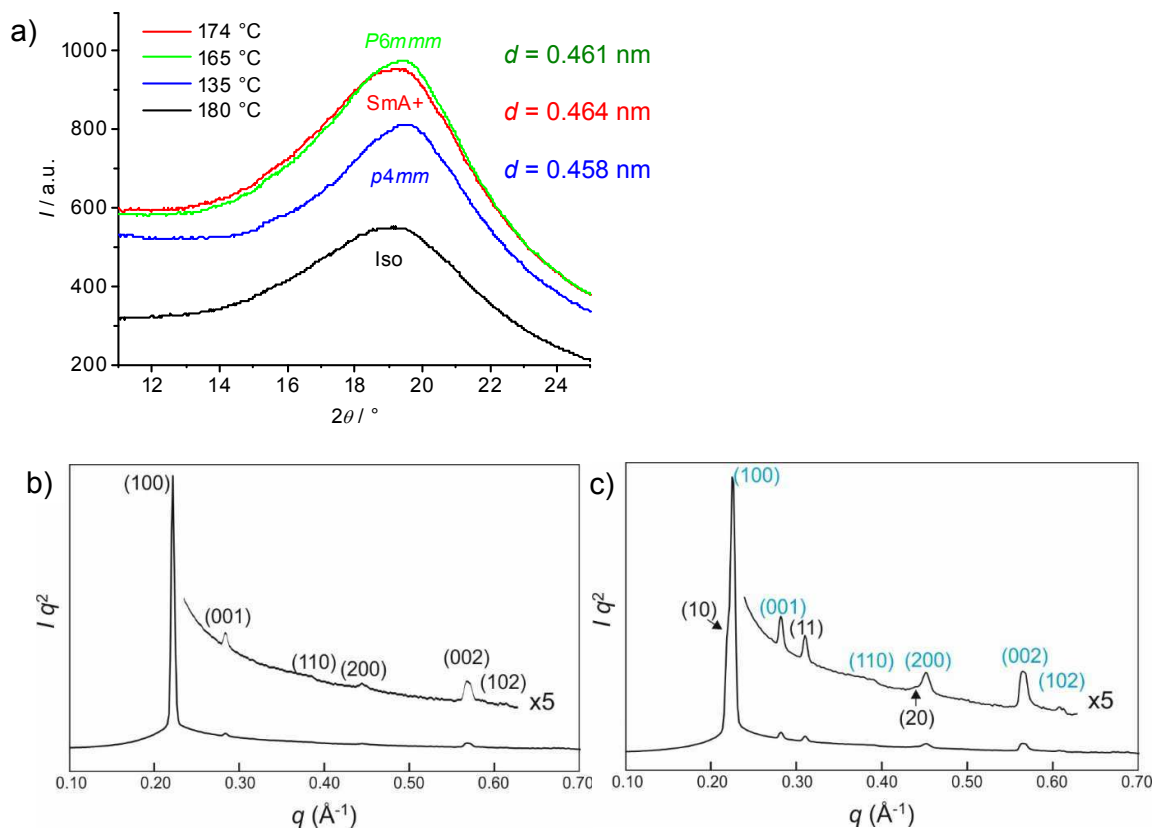


Figure S13. a) WAXS profiles on the distinct LC phases of compound **A12** and b) SAXS pattern of the $P6/mmm$ phase at 160 °C and c) of the $p4mm+P6/mmm$ range at 125 °C .

Table S5. Numerical XRD data of the LC phases of compound **A12**.

$P6/mmm$ phase at 160 °C ($a = 3.27$ nm, $c = 2.21$ nm).

d -exp (nm)	d -calc	(hkl)	Intensity
2.83	2.83	(100)	100
2.21	2.21	(001)	1.07
1.65	1.63	(110)	0.39
1.41	1.42	(200)	0.77
1.10	1.11	(002)	3.16
1.03	1.03	(102)	0.14

$p4mm$ phase at 125 °C ($a_{\text{squ}} = 2.86$ nm)

d -exp (nm)	d -calc	(hkl)	Intensity
2.86	2.86	(10)	100
2.02	2.02	(11)	4.42
1.43	1.43	(20)	1.41

2.3.7 Compound A13

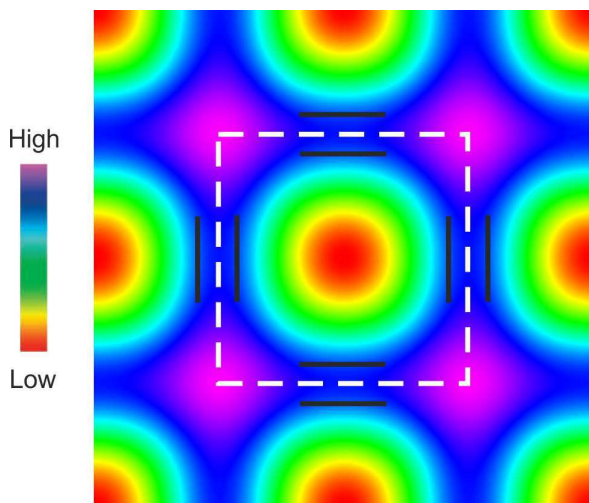


Figure S14. Reconstructed ED map of the $\text{Col}_{\text{rec}}/p4mm$ phase of **A13** at 130 °C using the data in Table S6b (black lines represent aromatics).

Table S6. Numerical XRD data of the LC phases of compound **A13**.

a) $P6/mmm$ phase at 145 °C ($a = 3.28$ nm, $c = 2.20$ nm)

d -exp (nm)	d -calc (nm)	(hkl)	Intensities
2.84	2.84	(100)	100
2.21	2.20	(001)	1.63
1.64	1.64	(110)	0.23
1.42	1.42	(200)	0.42
1.10	1.10	(002)	0.37

b) $p4mm$ phase at 130 °C ($a = 2.83$ nm)

d -exp (nm)	(hk)	d -calc (nm)	Intensities (phases)
2.82	(10)	2.83	100 (-)
2.02	(11)	2.00	8.31 (-)
1.41	(20)	1.42	0.45 (+)

2.3.8 Compound A14

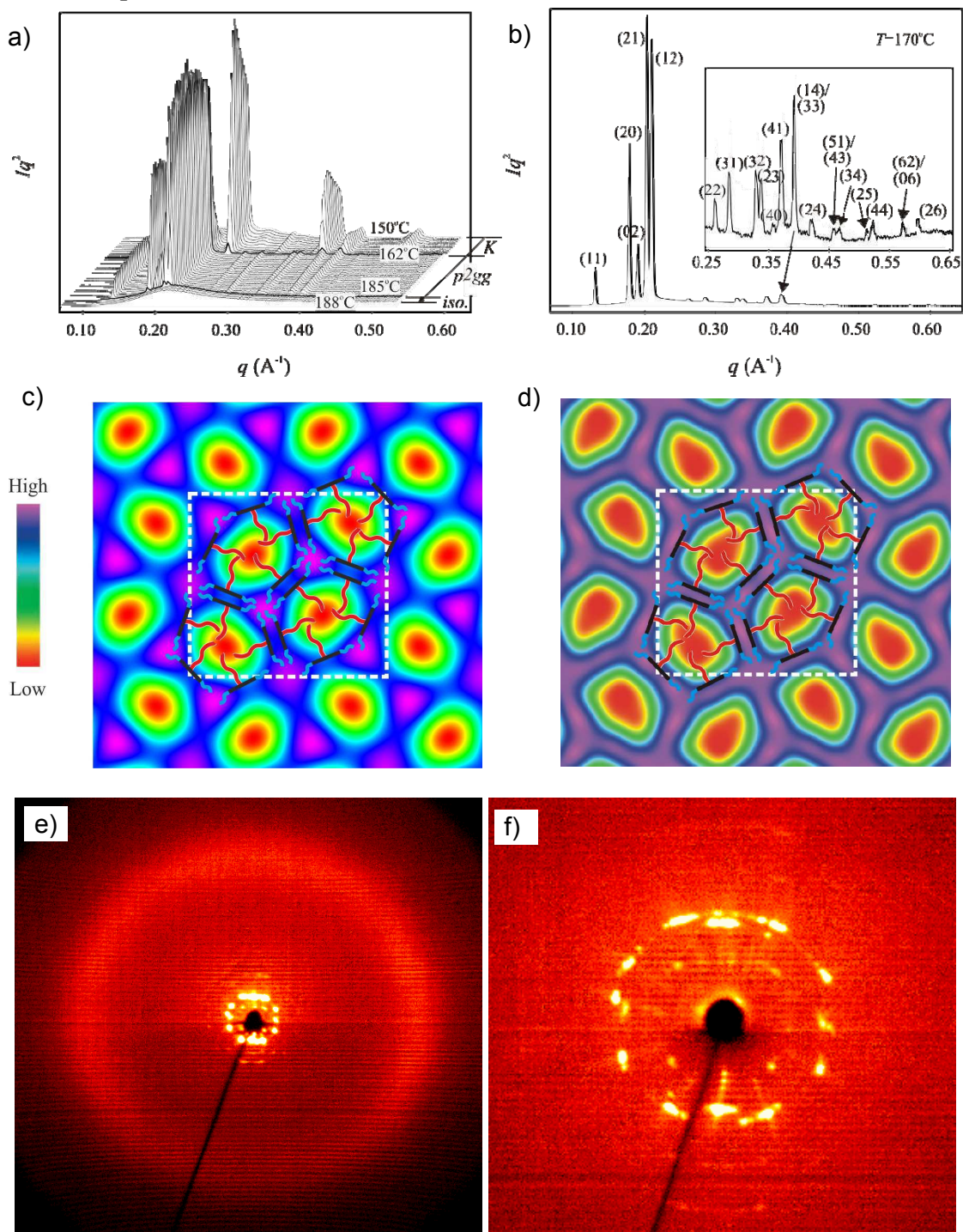


Figure S15. Diffraction patterns of **A14**. a) Temperature scan on cooling and b) diffraction pattern of the $p2gg$ phase at 170 °C; c) reconstructed electron density map of the $p2gg$ phase by using the first five diffractions and d) using all reflections (Table S8); e,f) 2D XRD pattern of an aligned sample of the $p2gg$ phase at $T = 175$ °C; e) WAXS (maximum of diffuse scattering at $d = 0.47$ nm) and f) SAXS pattern at $T = 120$ °C.

Table S7. Experimental and calculated d -spacings of the observed SAXS reflections (Fig. 15b; synchrotron source) of the rectangular $p2gg$ phase in compound **A14** at 170 °C. All intensities values are Lorentz corrected with correction for multiplicity.

(hk)	$d_{\text{obs.}}-\text{spacing (nm)}$	$d_{\text{cal.}}-\text{spacing (nm)}$	$intensity$	$phase$
(11)	4.79	4.79	10.4	π
(20)	3.50	3.50	94.3	0
(02)	3.29	3.29	36.5	0
(21)	3.09	3.09	95.3	π
(12)	2.98	2.98	100.0	π
(22)	2.40	2.40	1.0	0
(31)	2.20	2.20	2.0	0
(32)	1.90	1.90	2.2	0
(23)	1.86	1.86	2.1	0
(40)	1.75	1.75	0.4	0
(41)	1.69	1.69	4.0	π
(33)	1.60	1.60	2.8	0
(14)			2.8	π
(24)	1.49	1.49	0.6	0
(51)	1.37	1.37	0.1	π
(43)			0.1	π
(34)	1.35	1.34	0.5	π
(25)	1.23	1.23	0.1	π
(44)	1.20	1.20	0.5	π
(62)	1.10	1.10	0.1	π
(06)			0.3	π
(26)	1.05	1.05	0.3	π
$a = 7.00 \text{ nm}, b = 6.58 \text{ nm}$				

2.4. Structural parameters

Table S8. Lattice parameters and calculation of the molecular volume (V_{mol}), volume of the unit cells (V_{cell}), number of molecules in these unit cells (n_{cell}) and number of molecules in the lateral cross section of the honeycomb walls (n_{wall}).^a

Compd.	f_{R}	Phase	T (°C)	Lattice parameters (nm)	d_{diff} (nm)	V_{cell}	V_{mol} (nm ³)	n_{cell}	n_{wall}
A5	0.20	SmA+	170	$d_1 = 2.16, d_2 = 1.83^b$	0.46	-	-	-	-
A8	0.28	SmA+	130	$d_1 = 2.20, d_2 = 2.2^b$	0.46	-	-	-	-
A8		<i>P6/mmm</i>	110	$a_{\text{hex}} = 2.44, c = 2.20$	0.45	11.3	0.73	13.9	2.6
A9	0.31	SmA+	160	$d_1 = 2.19, d_2 = 2.32$	0.46	-	-	-	-
A9		<i>P6/mmm</i>	110	$a_{\text{hex}} = 2.64, c = 2.18$	0.45	13.2	0.75	15.7	2.6
A10	0.33	SmA+	165	$d_1 = 2.13, d_2 = 2.51^b$	0.46	-	-	-	-
A10		<i>P6/mmm</i>	153	$a_{\text{hex}} = 2.84, c = 2.17$	0.45	15.5	0.78	17.4	2.7
A10		<i>p4mm</i>	115	$a_{\text{squ}} = 2.81$	0.45	3.55	0.78	4.1	2.0
A11	0.35	SmA+	175	$d_1 = 2.16, d_2 = 2.66^b$	0.47	-	-	-	-
A11		<i>P6/mmm</i>	155	$a_{\text{hex}} = 3.05, c = 2.22$	0.46	17.9	0.80	20.0	2.7
A11		<i>p4mm</i>	120	$a_{\text{squ}} = 2.86$	0.45	3.68	0.80	4.1	2.0
A12	0.37	SmA+	174	$d_1 = 2.14, d_2 = 2.83^b$	0.46	-	-	-	-
A12		<i>P6/mmm</i>	160	$a_{\text{hex}} = 3.27, c = 2.21$	0.46	20.5	0.83	22.0	2.7
A12		<i>p4mm</i>	125	$a_{\text{squ}} = 2.86$	0.46	3.76	0.83	4.0	2.0
A13	0.39	SmA+	175	$d_1 = 2.12, d_2 = 2.84$	0.46	-	-	-	-
A13		<i>P6/mmm</i>	145	$a_{\text{hex}} = 3.28, c = 2.20$	0.46	20.5	0.85	21.5	2.7
A13		<i>P4mm</i>	130	$a_{\text{squ}} = 2.83$	0.46	3.68	0.85	3.9	1.9
A14	0.41	<i>p2gg</i>	115	$a = 7.00, b = 6.58$	0.47	21.6	0.88	22.0	2.2

^a f_{R} = volume fraction of the lateral alkyl chain; $V_{\text{cell}} = A_{\text{cell}} \times h$, where $A_{\text{cell}} = a_{\text{aqu}}^2$ for *p4mm*, and $a \times b$ for the rectangular phases; for the tangential-rod-honeycombs h corresponds to the d -value of the maximum of the diffuse wide angle scattering (d_{diff}). For the *P6/mmm* phases $V_{\text{cell}} = A_{\text{cell}} \times c$ (with $A_{\text{cell}} = \sqrt{3}/2 \times a_{\text{hex}}^2 = 0.866 a_{\text{hex}}^2$); V_{mol} = volume for a single molecule as calculated using crystal volume increments;^{S2} n_{cell} = number of molecules in the unit cell, calculated according to $n_{\text{cell}} = k \times V_{\text{cell}}/V_{\text{mol}}$ with $k = 0.893$, being a correction for the packing density in the LC state;^{S3} n_{wall} = average number of molecules in the cross section of the honeycomb walls as calculated for the tangential-rod-honeycombs from n_{cell} by dividing by the number of walls per unit cell (*p4mm*: 2, *p2gg*: 10) and for the coaxial rod honeycombs (*P6/mmm*) according to $n_{\text{wall}} = [a_{\text{hex}} - (2f_{\text{R}} \times A_{\text{cell}}/\sqrt{3})^{1/2}]/d_{\text{diff}}$; d_{diff} = position of the diffuse wide angle scattering maximum; for details of the calculations, see the following Section 2.5 and Fig. S16. ^b Diffuse small angle scattering.

2.5 Calculation of n_{wall} for the $P6/mmm$ phases

The volume of the alkyl chains in each unit cell (V_{R}) is the unit cell volume (V_{cell}) multiplied by the volume fraction of the lateral chains (f_{R}):

$$V_{\text{R}} = V_{\text{cell}} \times f_{\text{R}} = A_{\text{R}} \times c = A_{\text{cell}} \times c \times f_{\text{R}} \quad (1)$$

division by parameter c gives the corresponding areas:

$$A_{\text{R}} = A_{\text{cell}} \times f_{\text{R}} \quad (2)$$

Where A_{R} is the area of the lateral chains in each hexagonal 2d unit cell; A_{cell} is calculated from a_{hex} by: $A_{\text{cell}} = \sqrt{3}/2 \times a_{\text{hex}}^2$, and similarly, the area required by the alkyl chains A_{R} is calculated by $A_{\text{R}} = a_{\text{R}}^2 \times \sqrt{3}/2$ and therefrom it follows after transposition that

$$a_{\text{R}} = (2A_{\text{R}}/\sqrt{3})^{1/2} \quad (3)$$

(for definition of a_{R} , see Fig. S16a) replacing A_{R} by equ. (2) gives

$$a_{\text{R}} = (2f_{\text{R}} \times A_{\text{cell}}/\sqrt{3})^{1/2} \quad (4)$$

The thickness of the aromatic walls d_{wall} is the difference $d_{\text{wall}} = a_{\text{hex}} - a_{\text{R}}$ and according to equ (4):

$$d_{\text{wall}} = a_{\text{hex}} - a_{\text{R}} = a_{\text{hex}} - (2f_{\text{R}} \times A_{\text{cell}}/\sqrt{3})^{1/2} \quad (5)$$

d_{wall} divided by the average distance between the rotationally disordered aromatics, (position of the maximum of the diffuse wide angle scattering d_{diff}) gives the approximate number of molecules in the lateral cross section of the walls (the walls between two prismatic cells of the alkyl chains; the number of molecules in the diameter of shell around a single R_{H} column is $n_{\text{wall}}/2$) in the hexagonal coaxial-rod-honeycombs (n_{wall}) according to:

$$n_{\text{wall}} = d_{\text{wall}}/d_{\text{diff}} = [a_{\text{hex}} - (2f_{\text{R}} \times A_{\text{cell}}/\sqrt{3})^{1/2}]/d_{\text{diff}} \quad (6)$$

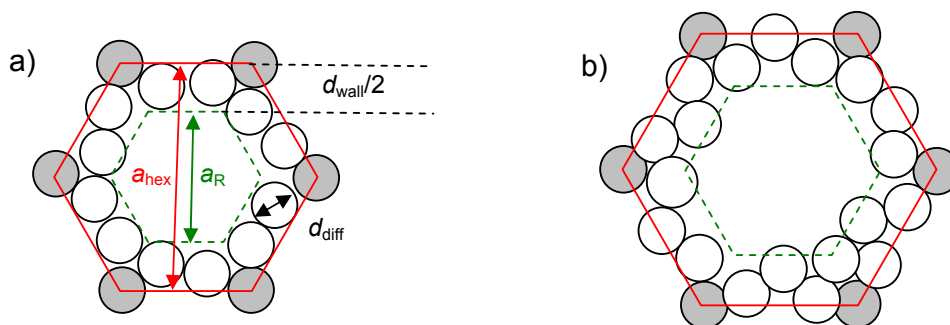


Figure S16. Cross section through one coaxial hexagonal honeycomb of the $P6/mmm$ phases (approximately in scale) of a) compound **A8** and b) compound **A13** with explanation of the dimensions used for calculations and the arrangement of 14 (12 white and 2 gray), and 21 (19 white and 2 gray) molecules per unit cell, respectively, leading to $n_{\text{wall}} = \sim 2.6-2.7$; ($d_{\text{wall}}/2 \sim 1.3$ molecules). The circles represent the cross sections through the preferably edge-to-face

organized and rotationally disordered terphenyls; each of the gray circles at the vertices is shared by three cells; the interior in the green dashed hexagon is filled by the alkyl chains.

2.6 Molecular models and MD simulations

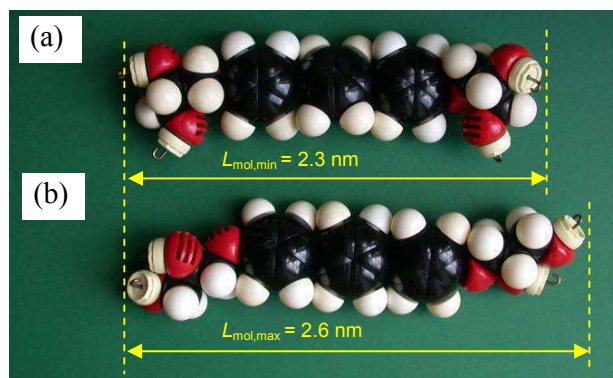


Figure S17. Molecular models showing compounds **An** (without lateral chain) in the conformations with a) minimized and b) maximized molecular length corresponding to $L_{\text{mol,min}} = 0.23$ nm and $L_{\text{mol,max}} = 0.26$ nm, respectively.



Figure S18. Some conformations of compound **A10**.

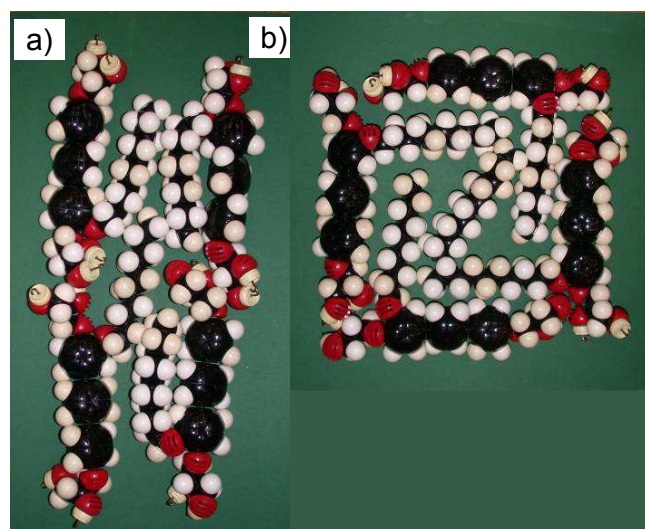


Figure S19. a) Model of a section of the channel structure in the $P6/mmm$ phase of **A10** and b) cross section through a square honeycomb cell of **A10** with different modes of preferred alkyl chain alignment (Fig. S18).

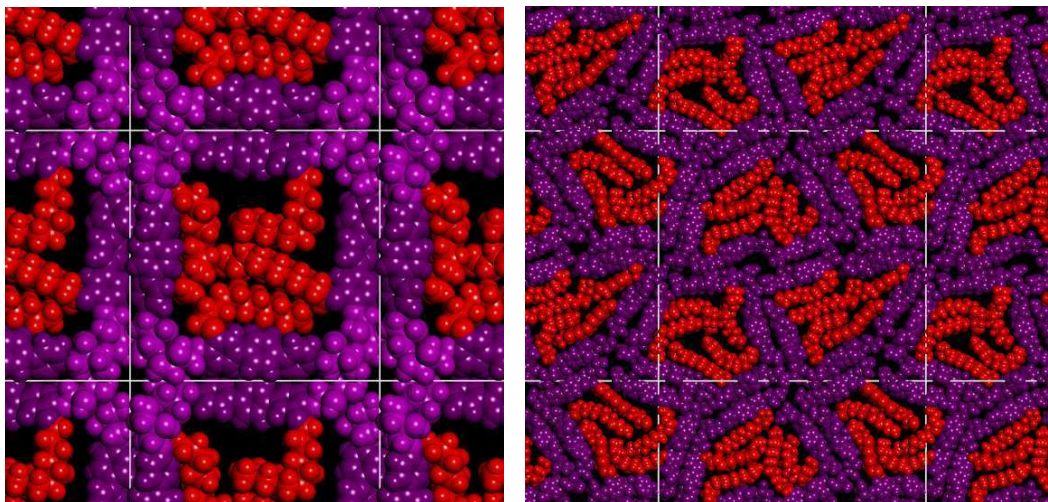
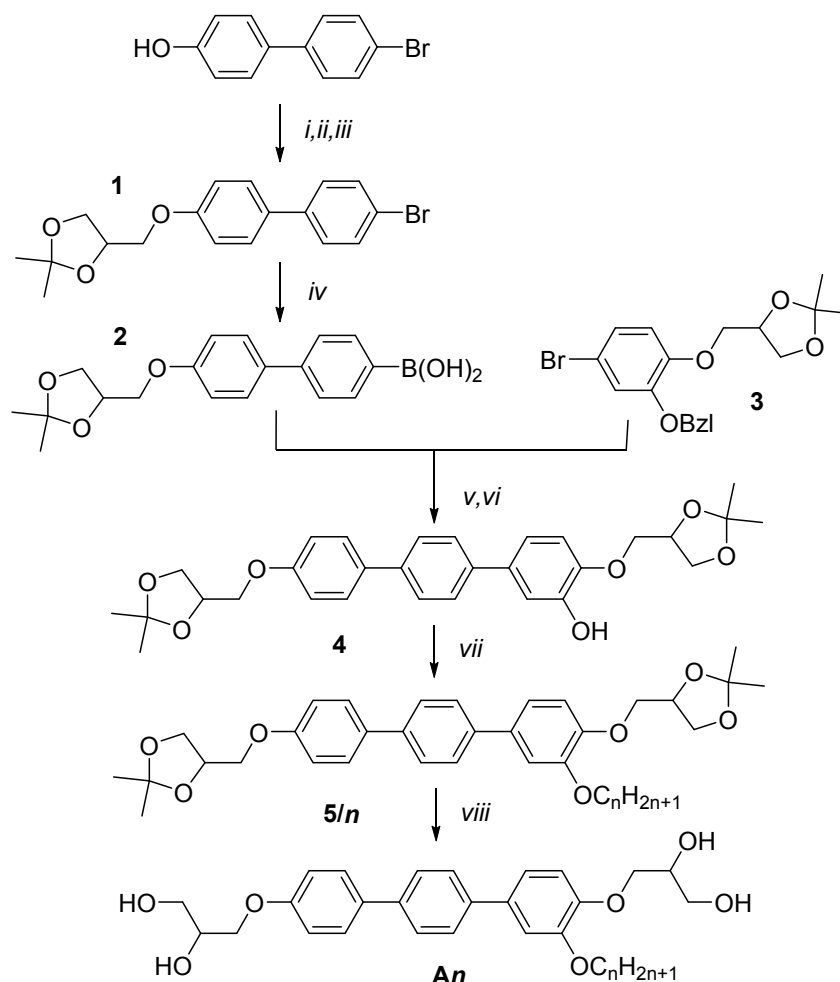


Figure S20. The snapshots of molecular dynamics simulations a) of Col_{sq}/p4mm phase of compound **A9**, and b) Col_{rec}/p2gg phase of **A14**; color coding is as follows: red = alkyl chains (lowest electron density), purple = terphenyl and glycerol groups (high density). In both tangential-rod-honeycombs the preferred orientation of the alkyl chains is parallel to the p-terphenyl cores in the walls.

3. Synthesis and analytical data

3.1 General

Synthesis of the compounds was performed according to Scheme S1 using the procedures described below. Unless otherwise noted, all starting materials were purchased from commercial sources and were used without further purification. Column chromatography was performed with silica gel 60 (63-200 μm , Merck). Determination of structures and purity of intermediates and products was obtained by NMR spectroscopy (VARIAN Gemini 200, Unity 500 and VRX 400, all spectra were recorded at 27 $^{\circ}\text{C}$) Microanalyses were performed using a CHNS-932 (Leco) elemental analyzer. The purity of all products was checked with thin layer chromatography (silicagel 60 F254, Merck). $\text{CHCl}_3/\text{EtOAc}$ mixtures and $\text{CHCl}_3/\text{MeOH}$ mixtures were used as eluents and the spots were detected by UV radiation or in I_2 vapour. All compounds represent racemic mixtures of diastereomers.



Scheme S1. Synthesis of compounds **An**. *Reagents and conditions:* i: $\text{CH}_2=\text{CH}-\text{CH}_2\text{Br}$, K_2CO_3 , 2-butanone, reflux, 6 h; ii: *N*-methylmorpholine-*N*-oxide (NMMNO), cat. OsO_4 , acetone, 20 $^{\circ}\text{C}$, 60 h;^{S4} iii: $\text{Me}_2\text{C}(\text{OMe})_2$, cat. pyridinium *p*-toluenesulfonate (PPTS);^{S5} iv: 1. *n*-Buli, -85 $^{\circ}\text{C}$, 2. $\text{B}(\text{OMe})_3$, -85 \rightarrow 20 $^{\circ}\text{C}$, 3. $\text{KH}_2\text{PO}_4/\text{Na}_2\text{HPO}_4/\text{H}_2\text{O}$ buffer;^{S9} v: cat. $\text{Pd}[\text{PPh}_3]_4$, NaHCO_3 , H_2O , glyme, reflux, 5 h;^{S6} vi: cyclohexene, cat. $\text{Pd}(\text{OH})_2/\text{C}$, THF, 20 $^{\circ}\text{C}$,

14 h,^{S7} vii: C_nH_{2n+1}Br, K₂CO₃, 2-butanone, reflux, 5h; viii: MeOH, THF, cat. PPTS, reflux, 6-24 h.⁸

n-Alkylbromides (Merck), 4'-bromobiphenyl-4-ol (Merck), trimethylborat (Merck), *n*-butyllithium 1.6 M in hexane (ACROS), glyme (Alfa Aesar), osmium tetroxide (Berlin Chemie), Pd(OH)₂ on charcoal (Fluka), pyridinium-*p*-toluene sulfonate (Merck) and *N*-methylmorpholine-*N*-oxide 50-wt.% in H₂O (Fluka) were used as received.

4'-[(2,2-Dimethyl-1,3-dioxolane-4-yl)methoxy]benzene-4-boronic acid (3) was prepared as described in ref.^{S9}: Colorless solid, mp.: 143-146 °C; ¹H-NMR (acetone-D₆, J/Hz, 400 MHz) δ = 7.81 (d, ³J(H,H) = 8.7, 2H, Ar-H), 6.92 (d, ³J(H,H) = 9.5, 2H, Ar-H), 4.44 (m, 1H, OCH), 4.14 (dd, ²J(H,H) = 8.3, ³J(H,H) = 6.4, 1H, OCH₂), 4.09 - 4.02 (m, 2H, OCH₂), 3.85 (dd, ²J(H,H) = 8.3, ³J(H,H) = 6.2, 1H, OCH₂), 1.37 (s, 3H, CH₃), 1.32 (s, 3H, CH₃).

3.2 Synthesis of 4,4''-bis[(2,2-dimethyl-1,3-dioxolane-4-yl)methoxy]-*p*-terphenyl-3-ol (4)

4-Allyloxy-4'-bromobiphenyl^{S10}

A mixture of 4'-bromobiphenyl-4-ol (25 g, 0.10 mol), allyl bromide (12 ml, 0.11 mol) and K₂CO₃ (27.6 g, 0.2 mol) in 2-butanone (250 ml) was stirred for 6 h under reflux. After cooling to room temperature, the reaction mixture was poured into ice-water (250 ml) and extracted with diethyl ether (3 x 100 ml). The combined organic layers were washed with water and brine. After drying over anhydrous Na₂SO₄, filtration and evaporation of the solvent, the crude product was used without further purification. Colorless solid; yield: 28.2 g (0.098 mol, 98 %); mp 124-128 °C; ¹H-NMR (CDCl₃, J/Hz, 400 MHz) δ = 7.50(d, ³J(H,H) = 8.5, 2H, Ar-H), 7.45 (d, ³J(H,H) = 8.7, 2H, Ar-H), 7.38 (d, ³J(H,H) = 8.5, 2H, Ar-H), 6.96 (d, ³J(H,H) = 8.7, 2H, Ar-H), 6.11 - 6.01 (m, 1H, CH = CH₂), 5.42 (dd, ²J(H,H) = 1.5, ³J(H,H) = 17.3, 1H, CH = CH₂), 5.29 (dd, ²J(H,H) = 1.2, ³J(H,H) = 10.2, 1H, CH = CH₂), 4.56 (d, ³J(H,H) = 5.2, 2H, OCH₂).

3-(4'-Bromobiphenyl-4-yloxy)propane-1,2-diol

To a mixture of 4-allyloxy-4'-bromobiphenyl (27.9 g, 0.097 mol) in acetone (200 ml) was added NMMO (13.8 g, 0.116 mol of a 50-wt% aq. solution) and OsO₄ (16 ml of a 0.004M solution in *tert*-butanol). The mixture was stirred at room temperature for 60 h and checked by TLC. After addition of saturated Na₂SO₃ solution in water (250 ml), the mixture was stirred for 1 h. The solution was diluted with water (500 ml) and extracted with Et₂O (3 x 100 ml). The combined organic layers were washed with 10 % aq. H₂SO₄, sat. aq. NaHCO₃, water and brine. After drying over anhydrous Na₂SO₄, filtration and evaporation of the solvent, the crude product was crystallized from EtOAc. Colorless solid; yield: 28.4 g (0.088 mol, 91 %), mp.: 178-180 °C; ¹H-NMR (DMSO-D₆, J/Hz, 400 MHz) δ = 7.58-7.53 (m, 6H, Ar-H), 6.99 (d, ³J(H,H) = 8.9, 2H, Ar-H), 4.91 (d, ³J(H,H) = 5.0, 1H, OH), 4.62 (t, ³J(H,H) = 5.6, 1H, OH), 4.01 (dd, ²J(H,H) = 9.9, ³J(H,H) = 4.2, 1H, OCH₂), 3.87 (dd, ²J(H,H) = 10.0, ³J(H,H) = 6.2, 1H, OCH₂), 3.78 (m, 1H, CHOH), 3.42 (dd, ³J(H,H) = 5.8, ³J(H,H) = 5.6, 2H, OCH₂).

4-(4'-Bromobiphenyl-4-yloxymethyl)-2,2-dimethyl-1,3-dioxolane (1)

A suspension of 3-(4'-bromobiphenyl-4-yloxy)propane-1,2-diol (16.5 g, 0.051 mol) and PPTS (0.1 g, 0.4 mmol) in 2,2-dimethoxypropane (200 ml) was stirred at room temperature for 60 h.

Thereafter, the solvent was evaporated and the residue was taken up in diethyl ether. The solution was washed with sat. aq. NaHCO₃, water and brine. After drying over anhydrous Na₂SO₄, the solvent was removed under reduced pressure and the crude product was purified by crystallization from CHCl₃ /n-hexane. Colorless solid; yield: 14.9 g (0.041 mol, 81 %); mp.: 103-106 °C; ¹H-NMR (CDCl₃, J/Hz, 400 MHz) δ = 7.51 (d, ³J(H,H) = 8.5, 2H, Ar-H), 7.46 (d, ³J(H,H) = 8.7, 2H, Ar-H), 7.39 (d, ³J(H,H) = 8.3, 2H, Ar-H), 6.96 (d, ³J(H,H) = 8.7, 2H, Ar-H), 4.48 (m, 1H, OCH), 4.17 (dd, ²J(H,H) = 8.4, ³J(H,H) = 6.4, 1H, OCH₂), 4.08 (dd, ²J(H,H) = 9.5, ³J(H,H) = 5.4, 1H, OCH₂), 3.96 (dd, ²J(H,H) = 9.5, ³J(H,H) = 5.8, 1H, OCH₂), 3.90 (dd, ²J(H,H) = 8.5, ³J(H,H) = 5.8, 1H, OCH₂), 1.46 (s, 3H, CH₃), 1.40 (s, 3H, CH₃).

4'-[(2,2-Dimethyl-1,3-dioxolane-4-yl)methoxy]biphenyl-4-ylboronic acid (2)

1 (14.9 g, 0.041 mol) was dissolved in dry THF (250 mL) under an argon atmosphere. The solution was cooled to -85 °C and n-BuLi (27.7 ml of a 1.6 M Lösung in n-hexane, 0.044 mol) was added dropwise at this temperature. After stirring at this temperature for additional 15 min, trimethylborate (15 ml, 0.124 mol) was carefully added dropwise, so that the temperature does not exceed -85 °C. Stirring was continued and the mixture was allowed to warm to ambient temperature overnight. Then phosphate-buffer (Sörensen, pH = 4.5 - 5.0; 81.6 ml KH₂PO₄-solution. + 0.8 ml Na₂HPO₄-solution) was added. After stirring for an additional hour, Et₂O (75 mL) was added and the layers were separated. The aqueous layer was extracted with Et₂O (4 x 50 mL). The combined organic layers were washed with water (3 x 20 mL) and brine (3 x 20 ml) and were dried with Na₂SO₄. After evaporation of the solvent the residue was suspended in hot CHCl₃. After cooling the precipitate was succed off. The crude product was used for the next step. Yield 12.8 g (0.039 mol, 95 %); colorless solid, mp.: 205-210 °C; ¹H-NMR (Aceton-D₆, J/Hz, 400 MHz) δ = 7.92 (d, ³J(H,H) = 8.3, 2H, Ar-H), 7.61 (d, ³J(H,H) = 8.9, 2H, Ar-H), 7.59 (d, ³J(H,H) = 8.3, 2H, Ar-H), 7.05 (d, ³J(H,H) = 8.9, 2H, Ar-H), 4.46 (m, 1H, OCH), 4.16 (dd, ²J(H,H) = 8.3, ³J(H,H) = 6.4, 1H, OCH₂), 4.11-4.06 (m, 2H, OCH₂), 3.87 (dd, ²J(H,H) = 8.3, ³J(H,H) = 6.2, 1H, OCH₂), 1.39 (s, 3H, CH₃), 1.33 (s, 3H, CH₃).

3-Benzyloxy-4,4''-bis[(2,2-dimethyl-1,3-dioxolane-4-yl)methoxy]-p-terphenyl (4-Bzl)

A mixture of **3** (10 g, 0.025 mol), **2** (9.18 g, 0.027 mol) Pd(PPh₃)₄, 1.5 g (1.27 mmol), glylme (150 ml) and sat. aq. NaHCO₃ (100 ml) was stirred under an argon atmosphere at reflux for 5 h. After cooling to room temperature the solvent was removed and the residue was extracted with CHCl₃ (3 x 50 ml). The combined organic layers were washed with water and brine. After drying over anhydrous Na₂SO₄, the solvent was removed under reduced pressure, the residue was purified by column chromatography (eluent: CH₂Cl₂ /Et₂O, 97:3, V/V) and crystallized from CDCl₃/n-hexane (1:1, v/v). Colorless solid; yield: 10.5 g (17.6 mmol, 69 %); mp 125-128 °C; ¹H-NMR (CDCl₃, J/Hz, 400 MHz) δ = 7.58-7.52 (m, 6H, Ar-H), 7.45 (d, ³J(H,H) = 7.1, 2H, Ar-H), 7.41-7.28 (m, 3H, Ar-H), 7.21-7.15 (m, 2H, Ar-H), 7.02-6.97 (m, 3H, Ar-H), 5.16 (s, 2H, OCH₂Ph), 4.49 (m, 2H, OCH), 4.19-3.90 (m, 8H, OCH₂), 1.47 (s, 3H, CH₃), 1.43 (s, 3H, CH₃), 1.40 (s, 3H, CH₃), 1.38 (s, 3H, CH₃).

4,4''-Bis[(2,2-dimethyl-1,3-dioxolane-4-yl)methoxy]-p-terphenyl-3-ol (4)

4-Bzl (10.5 g, 17.6 mmol) was dissolved in THF (150 ml). Under an argon atmosphere cyclohexene (40 ml) and Pd(OH)₂/C (0.6 g; 10% Pd) were added. The reaction mixture as refluxed for 14 h; the catalyst was filtered off and washed with hot THF. The solvent was evaporated and the crude product was purified by crystallization from THF/CHCl₃. Colorless solid; yield: 8.8 g (17.3 mmol, 98 %); mp.: 204-207 °C; ¹H-NMR (CDCl₃, J/Hz, 400 MHz) δ

= 7.58 (s, 4H, Ar-H), 7.54 (d, $^3J(\text{H,H}) = 8.7$, 2H, Ar-H), 7.22 (d, $^4J(\text{H,H}) = 2.3$, 1H, Ar-H), 7.08 (dd, $^3J(\text{H,H}) = 8.3$, $^4J(\text{H,H}) = 2.3$, 1H, Ar-H), 6.99-6.95 (m, 3H, Ar-H), 6.20 (s, 1H, OH), 4.49 (m, 2H, OCH), 4.19-4.05 (m, 5H, OCH₂), 3.97 (dd, $^2J(\text{H,H}) = 9.5$, $^3J(\text{H,H}) = 6.0$, 1H, OCH₂), 3.93-3.89 (m, 2H, OCH₂), 1.49 (s, 3H, CH₃), 1.46 (s, 3H, CH₃), 1.41 (s, 3H, CH₃), 1.40 (s, 3H, CH₃).

3.3 4,4''-Bis[(2,2-dimethyl-1,3-dioxolane-4-yl)methoxy]-3-alkoxy-p-terphenyls (5/n)

General procedure. - A mixture of **4** (1 eq.), 1-bromo n-alkane (1.1 eq.), K₂CO₃ (2 eq.) and tetrabutylammonium iodide (5 mg) in anhydrous MeCN (50 ml for each mmol **4**) was stirred under reflux for 6-24 h. After complete consumption of **4** (DC) the mixture was cooled to room temperature, the reaction mixture was poured into ice-water (50 ml) and the aqueous layer was extracted with diethyl ether (2 x 50 mL). The combined organic layers were washed with water (50 ml) and brine (50 ml). After drying over anhydrous Na₂SO₄, filtration and evaporation of the solvent, the crude product was purified by chromatography or crystallization.

4,4''-Bis[(2,2-dimethyl-1,3-dioxolane-4-yl)methoxy]-3-pentyloxy-p-terphenyl 5/5

Purified by crystallization from CHCl₃ /n-hexane, yield 89 %; colorless solid; mp.: 99-101 °C; C₃₅H₄₄O₇, M=576.72 g/mol; ¹H-NMR (CDCl₃, J/Hz, 400 MHz) δ = 7.58 (s, 4H, Ar-H), 7.54 (d, $^3J(\text{H,H}) = 8.7$, 2H, Ar-H), 7.14-7.11 (m, 2H, Ar-H), 6.98 (dd, $^3J(\text{H,H}) = 8.7$, $^4J(\text{H,H}) = 1.5$, 3H, Ar-H), 4.49 (m, 2H, OCH), 4.19-3.96 (m, 9H, OCH₂), 3.91 (dd, $^2J(\text{H,H}) = 8.5$, $^3J(\text{H,H}) = 5.8$, 1H, OCH₂), 1.83 (tt, $^3J(\text{H,H}) = 6.6$, $^3J(\text{H,H}) = 6.1$, 2H, OCH₂CH₂), 1.47 (s, 3H, CH₃), 1.46 (s, 3H, CH₃), 1.46 (m, 2H, OCH₂CH₂CH₂), 1.40 (s, 3H, CH₃), 1.40 (s, 3H, CH₃), 1.40 (m, 2H, OCH₂CH₂CH₂CH₂), 0.93 (t, $^3J(\text{H,H}) = 7.3$, 3H, CH₃).

4,4''-Bis[(2,2-dimethyl-1,3-dioxolane-4-yl)methoxy]-3-heptyloxy-p-terphenyl 5/7

Purified by column chromatography (CH₂Cl₂/ Et₂O, 98:2, V/V); yield 87 %; colorless solid; mp.: 93-95 °C; C₃₇H₄₈O₇, M=604.77 g/mol; ¹H-NMR (CDCl₃, J/Hz, 400 MHz) δ = 7.58 (s, 4H, Ar-H), 7.54 (d, $^3J(\text{H,H}) = 8.9$, 2H, Ar-H), 7.14-7.11 (m, 2H, Ar-H), 6.98 (d, $^3J(\text{H,H}) = 8.9$, 3H, Ar-H), 4.49 (m, 2H, OCH), 4.46-3.96 (m, 9H, OCH₂), 3.91 (dd, $^2J(\text{H,H}) = 8.5$, $^3J(\text{H,H}) = 5.8$, 1H, OCH₂), 1.82 (tt, $^3J(\text{H,H}) = 7.1$, $^3J(\text{H,H}) = 7.9$, 2H, OCH₂CH₂), 1.47 (s, 3H, CH₃), 1.46 (s, 3H, CH₃), 1.46 (m, 2H, OCH₂CH₂CH₂), 1.40 (s, 3H, CH₃), 1.40 (s, 3H, CH₃), 1.38-1.28 (m, 6H, CH₂), 0.88 (t, $^3J(\text{H,H}) = 6.8$, 3H, CH₃).

4,4''-Bis[(2,2-dimethyl-1,3-dioxolane-4-yl)methoxy]-3-octyloxy-p-terphenyl 5/8

Purified by column chromatography (CH₂Cl₂/ Et₂O, 98:2, V/V); yield 85 %; colorless solid; mp.: 84-86 °C; C₃₈H₅₀O₇, M=618.8 g/mol; ¹H-NMR (CDCl₃, J/Hz, 400 MHz) δ = 7.58 (s, 4H, Ar-H), 7.54 (d, $^3J(\text{H,H}) = 8.9$, 2H, Ar-H), 7.14-7.11 (m, 2H, Ar-H), 6.98 (dd, $^3J(\text{H,H}) = 8.8$, $^4J(\text{H,H}) = 1.5$, 3H, Ar-H), 4.49 (m, 2H, OCH), 4.19-3.96 (m, 9H, OCH₂), 3.91 (dd, $^2J(\text{H,H}) = 8.5$, $^3J(\text{H,H}) = 5.8$, 1H, OCH₂), 1.82 (tt, $^3J(\text{H,H}) = 6.8$, $^3J(\text{H,H}) = 7.9$, 2H, OCH₂CH₂), 1.47 (s, 3H, CH₃), 1.46 (s, 3H, CH₃), 1.46 (m, 2H, OCH₂CH₂CH₂), 1.40 (s, 3H, CH₃), 1.39 (s, 3H, CH₃), 1.32-1.28 (m, 8H, CH₂), 0.87 (t, $^3J(\text{H,H}) = 6.8$, 3H, CH₃).

4,4''-Bis[(2,2-dimethyl-1,3-dioxolane-4-yl)methoxy]-3-nonyloxy-p-terphenyl 5/9

Purified by column chromatography (CH₂Cl₂/ Et₂O, 97:3, V/V); yield 85 %; colorless solid; mp.: 88-90 °C; C₃₉H₅₂O₇, M=632.83 g/mol; ¹H-NMR (CDCl₃, J/Hz, 400 MHz) δ = 7.58 (s,

4H, Ar-H), 7.54 (d, $^3J(\text{H,H}) = 8.9$, 2H, Ar-H), 7.13-7.11 (m, 2H, Ar-H), 6.98 (d, $^3J(\text{H,H}) = 8.7$, 3H, Ar-H), 4.49 (m, 2H, OCH), 4.19-3.96 (m, 9H, OCH₂), 3.91 (dd, $^2J(\text{H,H}) = 8.3$, $^3J(\text{H,H}) = 5.8$, 1H, OCH₂), 1.82 (tt, $^3J(\text{H,H}) = 6.9$, $^3J(\text{H,H}) = 7.9$, 2H, OCH₂CH₂), 1.47 (s, 3H, CH₃), 1.46 (s, 3H, CH₃), 1.46 (m, 2H, OCH₂CH₂CH₂), 1.40 (s, 3H, CH₃), 1.40 (s, 3H, CH₃), 1.35-1.28 (m, 10H, CH₂), 0.87 (t, $^3J(\text{H,H}) = 6.6$, 3H, CH₃).

3-Decyloxy-4,4''-bis[(2,2-dimethyl-1,3-dioxolane-4-yl)methoxy]-p-terphenyl 5/10

Purified by column chromatography (CH₂Cl₂/ Et₂O, 98:2, V/V); yield 71 %; colorless solid; mp.: 92-95 °C; C₄₀H₅₄O₇, M=646.85 g/mol; ¹H-NMR (CDCl₃, J/Hz, 400 MHz) δ = 7.58 (s, 4H, Ar-H), 7.54 (d, $^3J(\text{H,H}) = 8.9$, 2H, Ar-H), 7.13-7.11 (m, 2H, Ar-H), 6.98 (dd, $^3J(\text{H,H}) = 8.7$, $^4J(\text{H,H}) = 1.5$, 3H, Ar-H), 4.49 (m, 2H, OCH), 4.20-3.96 (m, 9H, OCH₂), 3.91 (dd, $^2J(\text{H,H}) = 8.5$, $^3J(\text{H,H}) = 5.8$, 1H, OCH₂), 1.82 (tt, $^3J(\text{H,H}) = 7.1$, $^3J(\text{H,H}) = 7.9$, 2H, OCH₂CH₂), 1.47 (s, 3H, CH₃), 1.46 (s, 3H, CH₃), 1.46 (m, 2H, OCH₂CH₂CH₂), 1.40 (s, 3H, CH₃), 1.40 (s, 3H, CH₃), 1.30-1.26 (m, 12H, CH₂), 0.87 (t, $^3J(\text{H,H}) = 6.6$, 3H, CH₃).

4,4''-Bis[(2,2-dimethyl-1,3-dioxolane-4-yl)methoxy]-3-undecyloxy-p-terphenyl 5/11

Purified by column chromatography (CH₂Cl₂/ Et₂O, 97:3, V/V); yield 84 %; colorless solid; mp.: 93-95 °C; C₄₁H₅₆O₇, M=660.88 g/mol; ¹H-NMR (CDCl₃, J/Hz, 400 MHz) δ = 7.58 (s, 4H, Ar-H), 7.54 (d, $^3J(\text{H,H}) = 8.9$, 2H, Ar-H), 7.13-7.11 (m, 2H, Ar-H), 6.98 (dd, $^3J(\text{H,H}) = 8.7$, $^4J(\text{H,H}) = 1.5$, 3H, Ar-H), 4.49 (m, 2H, OCH), 4.47-3.96 (m, 9H, OCH₂), 3.91 (dd, $^2J(\text{H,H}) = 8.5$, $^3J(\text{H,H}) = 5.8$, 1H, OCH₂), 1.82 (tt, $^3J(\text{H,H}) = 7.1$, $^3J(\text{H,H}) = 7.7$, 2H, OCH₂CH₂), 1.47 (s, 3H, CH₃), 1.46 (s, 3H, CH₃), 1.46 (m, 2H, OCH₂CH₂CH₂), 1.40 (s, 3H, CH₃), 1.40 (s, 3H, CH₃), 1.25 (bs, 14H, CH₂), 0.86 (t, $^3J(\text{H,H}) = 6.6$, 3H, CH₃).

4,4''-Bis[(2,2-dimethyl-1,3-dioxolane-4-yl)methoxy]-3-dodecyloxy-p-terphenyl 5/12

Used without further purification for the next step; yield 78 %; colorless solid; mp.: 94-97 °C; C₄₂H₅₈O₇, M=674.91 g/mol; ¹H-NMR (CDCl₃, J/Hz, 400 MHz) δ = 7.58 (s, 4H, Ar-H), 7.54 (d, $^3J(\text{H,H}) = 8.7$, 2H, Ar-H), 7.14-7.11 (m, 2H, Ar-H), 6.98 (dd, $^3J(\text{H,H}) = 8.7$, $^4J(\text{H,H}) = 1.5$, 3H, Ar-H), 4.49 (m, 2H, OCH), 4.20-3.96 (m, 9H, OCH₂), 3.91 (dd, $^2J(\text{H,H}) = 8.3$, $^3J(\text{H,H}) = 5.8$, 1H, OCH₂), 1.82 (tt, $^3J(\text{H,H}) = 7.1$, $^3J(\text{H,H}) = 7.7$, 2H, OCH₂CH₂), 1.47 (s, 3H, CH₃), 1.46 (s, 3H, CH₃), 1.46 (m, 2H, OCH₂CH₂CH₂), 1.40 (s, 3H, CH₃), 1.40 (s, 3H, CH₃), 1.35-1.25 (m, 16H, CH₂), 0.86 (t, $^3J(\text{H,H}) = 6.6$, 3H, CH₃).

4,4''-Bis[(2,2-dimethyl-1,3-dioxolane-4-yl)methoxy]-3-tridecyloxy-p-terphenyl 5/13

Purified by column chromatography (CH₂Cl₂/ Et₂O, 98:2, V/V); yield 74 %; colorless solid; mp.: 92-95 °C; C₄₃H₆₀O₇, M=688.93 g/mol; ¹H-NMR (CDCl₃, J/Hz, 400 MHz) δ = 7.58 (s, 4H, Ar-H), 7.54 (d, $^3J(\text{H,H}) = 8.7$, 2H, Ar-H), 7.24-7.12 (m, 2H, Ar-H), 6.98 (dd, $^3J(\text{H,H}) = 8.7$, $^4J(\text{H,H}) = 1.3$, 3H, Ar-H), 4.49 (m, 2H, OCH), 4.19-3.96 (m, 9H, OCH₂), 3.91 (dd, $^2J(\text{H,H}) = 8.5$, $^3J(\text{H,H}) = 5.8$, 1H, OCH₂), 1.82 (tt, $^3J(\text{H,H}) = 7.5$, $^3J(\text{H,H}) = 7.3$, 2H, OCH₂CH₂), 1.47 (s, 3H, CH₃), 1.46 (s, 3H, CH₃), 1.46 (m, 2H, OCH₂CH₂CH₂), 1.40 (s, 3H, CH₃), 1.40 (s, 3H, CH₃), 1.35-1.25 (m, 18H, CH₂), 0.86 (t, $^3J(\text{H,H}) = 6.7$, 3H, CH₃).

4,4''-Bis[(2,2-dimethyl-1,3-dioxolane-4-yl)methoxy]-3-tetradecyloxy-p-terphenyl 5/14

Purified by column chromatography (CH₂Cl₂/ Et₂O, 98:2, V/V); yield 72 %; colorless solid; mp.: 88-90 °C; C₄₄H₆₂O₇, M=702.96 g/mol; ¹H-NMR (CDCl₃, J/Hz, 400 MHz) δ = 7.58 (s, 4H, Ar-H), 7.54 (d, $^3J(\text{H,H}) = 8.7$, 2H, Ar-H), 7.13-7.11 (m, 2H, Ar-H), 6.98 (d, $^3J(\text{H,H}) =$

8.7, 3H, Ar-H), 4.49 (m, 2H, OCH), 4.19-3.96 (m, 9H, OCH₂), 3.91 (dd, ²J(H,H) = 8.5, ³J(H,H) = 5.8, 1H, OCH₂), 1.82 (tt, ³J(H,H) = 6.8, ³J(H,H) = 7.9, 2H, OCH₂CH₂), 1.47 (s, 3H, CH₃), 1.46 (s, 3H, CH₃), 1.46 (m, 2H, OCH₂CH₂CH₂), 1.40 (s, 3H, CH₃), 1.39 (s, 3H, CH₃), 1.35-1.24 (m, 20H, CH₂), 0.86 (t, ³J(H,H) = 6.4, 3H, CH₃).

3.4 4,4''-Bis(2,3-dihydroxypropyloxy)-3-alkoxy-p-terphenyls A/n

A mixture of **5/n** (~ 0.5 mmol) and PPTS (20 mg) in MeOH/THF (30 mL/20 ml) was heated to reflux for 6-24 h. The progress of the reaction was monitored by TLC. After cooling to 20 °C water (200 ml) was added and the mixture was extracted with CHCl₃ until all precipitate is dissolved (~3 x 50 ml). The organic solutions were washed with water (50 ml), sat. NaHCO₃ (50 ml) and brine (50 mL). The solvent was evaporated and the crude product was purified by repeated crystallization.

4,4''-Bis(2,3-dihydroxypropyloxy)-3-pentyloxy-p-terphenyl A5

Purified by crystallization from MeOH/THF; yield 74 %; colorless solid; C₂₉H₃₆O₇, M=496.59 g/mol; ¹H-NMR (DMSO-D₆, J/Hz, 400 MHz) δ = 7.66-7.64 (m, 4H, Ar-H), 7.60 (d, ³J(H,H) = 8.7, 2H, Ar-H), 7.22 (d, ⁴J(H,H) = 2.1, 1H, Ar-H), 7.18 (dd, ³J(H,H) = 8.3, ⁴J(H,H) = 2.1, 1H, Ar-H), 7.01 (t, ³J(H,H) = 8.5, 3H, Ar-H), 4.91 (d, ³J(H,H) = 5.0, 1H, OH), 4.83 (d, ³J(H,H) = 5.2, 1H, OH), 4.62 (t, ³J(H,H) = 5.6, 1H, OH), 4.56 (t, ³J(H,H) = 5.6, 1H, OH), 4.05-3.95 (m, 4H, OCH, OCH₂), 3.90-3.86 (m, 2H, OCH₂), 3.80-3.76 (m, 2H, OCH₂), 3.49-3.41 (m, 4H, OCH₂), 1.72 (tt, ³J(H,H) = 6.8, ³J(H,H) = 7.5, 2H, OCH₂CH₂), 1.44-1.31 (m, 4H, CH₂), 0.88 (t, ³J(H,H) = 7.3, 3H, CH₃). ¹³C-NMR (DMSO-D₆, 100 MHz) δ = 158.2, 149.4, 138.7, 138.6, 132.4, 128.0, 127.2, 126.9, 119.4, 115.5, 115.1, 71.3, 70.6, 70.5, 70.3, 69.2, 63.5, 63.3, 29.2, 28.4, 22.5, 14.6. Analysis: calcd. for C₂₉H₃₆O₇*0.6 H₂O: C 68.64 %, H 7.39 %, found.: C 68.65 %, H 7.29 %.

4,4''-Bis(2,3-dihydroxypropyloxy)-3-heptyloxy-p-terphenyl A7

Purified by crystallization from MeOH/THF; yield 79 %; colorless solid; M=524.65 g/mol; ¹H-NMR (DMSO-D₆, J/Hz, 400 MHz) δ = 7.67-7.64 (m, 4H, Ar-H), 7.60 (d, ³J(H,H) = 8.7, 2H, Ar-H), 7.21 (d, ⁴J(H,H) = 1.9, 1H, Ar-H), 7.18 (dd, ³J(H,H) = 8.3, ⁴J(H,H) = 2.1, 1H, Ar-H), 7.01 (t, ³J(H,H) = 8.1, 3H, Ar-H), 4.05-3.95 (m, 4H, OCH, OCH₂), 3.90-3.86 (m, 2H, OCH₂), 3.81-3.76 (m, 2H, OCH₂), 3.49-3.40 (m, 4H, OCH₂), 1.71 (tt, ³J(H,H) = 7.1, ³J(H,H) = 7.7, 2H, OCH₂CH₂), 1.41 (m, 2H, OCH₂CH₂CH₂), 1.33-1.24 (m, 6H, CH₂), 0.84 (t, ³J(H,H) = 6.6, 3H, CH₃). ¹³C-NMR (DMSO-D₆, 100 MHz) δ = 158.2, 148.7, 148.2, 138.0, 137.9, 132.6, 131.7, 127.3, 126.5, 126.2, 118.7, 114.8, 114.5, 112.3, 70.7, 69.9, 69.9, 69.6, 68.5, 62.8, 62.6, 31.2, 28.8, 28.4, 25.4, 22.0, 13.9. Analysis: calcd. for C₃₁H₄₀O₇: C 70.97 %, H 7.68 %, found: C 70.62 %, H 7.67 %.

4,4''-Bis(2,3-dihydroxypropyloxy)-3-octyloxy-p-terphenyl A8

Purified by crystallization from MeOH/THF; yield 80 %; colorless solid; C₃₂H₄₂O₇, M=538.67 g/mol; ¹H-NMR (DMSO-D₆, J/Hz, 400 MHz) δ = 7.67-7.64 (m, 4H, Ar-H), 7.60 (d, ³J(H,H) = 8.7, 2H, Ar-H), 7.21 (d, ⁴J(H,H) = 2.1, 1H, Ar-H), 7.18 (dd, ³J(H,H) = 8.3, ⁴J(H,H) = 2.1, 1H, Ar-H), 7.00 (t, ³J(H,H) = 8.3, 3H, Ar-H), 4.91 (d, ³J(H,H) = 5.2, 1H, OH), 4.83 (d, ³J(H,H) = 5.2, 1H, OH), 4.63 (t, ³J(H,H) = 5.6, 1H, OH), 4.56 (t, ³J(H,H) = 5.6, 1H, OH), 4.05-3.95 (m, 4H, OCH, OCH₂), 3.90-3.86 (m, 2H, OCH₂), 3.80-3.75 (m, 2H, OCH₂), 3.47-3.41 (m, 4H, OCH₂), 1.70 (tt, ³J(H,H) = 6.8, ³J(H,H) = 7.7, 2H, OCH₂CH₂), 1.41 (m, 2H, OCH₂CH₂CH₂), 1.34-1.24 (m, 8H, CH₂), 0.83 (t, ³J(H,H) = 6.4, 3H, CH₃). ¹³C-NMR (DMSO-

D₆, 100 MHz) δ = 158.2, 148.7, 148.2, 138.0, 137.9, 132.6, 131.7, 127.3, 126.5, 126.2, 118.7, 114.8, 114.4, 112.2, 70.6, 69.9, 69.8, 69.6, 68.5, 62.8, 62.6, 31.1, 28.8, 28.7, 28.6, 25.4, 22.0, 13.9. Analysis: calcd for C₃₂H₄₂O₇: C 71.35 %, H 7.86 %, found: C 71.10 %, H 7.80 %.

4,4''-Bis(2,3-dihydroxypropyloxy)-3-nonyloxy-p-terphenyl A9

Purified by crystallization from EtOH; yield 83 %; colorless solid; C₃₃H₄₄O₇, M=552.70 g/mol; ¹H-NMR (DMSO-D₆, J/Hz, 400 MHz) δ = 7.69-7.66 (m, 4H, Ar-H), 7.62 (d, ³J(H,H) = 8.7, 2H, Ar-H), 7.24 (s, 1H, Ar-H), 7.21 (d, ³J(H,H) = 8.3, 1H, Ar-H), 7.04 (t, ³J(H,H) = 8.1, 3H, Ar-H), 4.07-3.98 (m, 4H, OCH, OCH₂), 3.93-3.88 (m, 2H, OCH₂), 3.82-3.78 (m, 2H, OCH₂), 3.49-3.45 (m, 4H, OCH₂), 1.73 (tt, ³J(H,H) = 6.9, ³J(H,H) = 7.5, 2H, OCH₂CH₂), 1.44 (m, 2H, OCH₂CH₂CH₂), 1.33-1.26 (m, 10H, CH₂), 0.85 (t, ³J(H,H) = 6.4, 3H, CH₃). ¹³C-NMR (DMSO-D₆, 100 MHz) δ = 158.2, 148.7, 148.2, 138.0, 137.9, 132.6, 131.7, 127.3, 126.5, 126.2, 118.7, 114.8, 114.5, 112.3, 70.6, 69.9, 69.8, 69.6, 68.5, 62.8, 62.6, 31.2, 28.9, 28.8, 28.7, 28.5, 25.4, 22.0, 13.9. Analysis: calcd. for C₃₃H₄₄O₇*0.15 H₂O: C 71.36 %, H 8.04 %, found: C 71.34 %, H 7.97 %.

3-Decyloxy-4,4''-bis(2,3-dihydroxypropyloxy)-p-terphenyl A10

Purified by crystallization from MeOH/THF; yield 89 %; colorless solid; C₃₄H₄₆O₇, M=566.72 g/mol; ¹H-NMR (DMSO-D₆, J/Hz, 400 MHz) δ = 7.67-7.63 (m, 4H, Ar-H), 7.60 (d, ³J(H,H) = 8.9, 2H, Ar-H), 7.21 (d, ⁴J(H,H) = 2.1, 1H, Ar-H), 7.18 (dd, ³J(H,H) = 8.3, ⁴J(H,H) = 2.1, 1H, Ar-H), 7.01 (t, ³J(H,H) = 8.1, 3H, Ar-H), 4.91 (d, ³J(H,H) = 5.0, 1H, OH), 4.83 (d, ³J(H,H) = 4.8, 1H, OH), 4.63 (t, ³J(H,H) = 5.6, 1H, OH), 4.56 (t, ³J(H,H) = 5.6, 1H, OH), 4.05-3.95 (m, 4H, OCH, OCH₂), 3.90-3.85 (m, 2H, OCH₂), 3.80-3.74 (m, 2H, OCH₂), 3.49-3.39 (m, 4H, OCH₂), 1.70 (tt, ³J(H,H) = 7.1, ³J(H,H) = 7.5, 2H, OCH₂CH₂), 1.41 (m, 2H, OCH₂CH₂CH₂), 1.34-1.20 (m, 12H, CH₂), 0.81 (t, ³J(H,H) = 6.6, 3H, CH₃). ¹³C-NMR (DMSO-D₆, 100 MHz) δ = 156.5, 147.1, 146.6, 136.4, 136.3, 130.9, 130.1, 125.6, 124.8, 124.5, 117.1, 113.2, 112.8, 110.7, 69.0, 68.3, 69.2, 68.0, 66.0, 61.1, 61.0, 29.5, 27.3, 27.2, 27.2, 27.0, 27.0, 23.8, 20.4, 12.2. Analysis: calcd. for C₃₄H₄₆O₇: C 72.06 %, H 8.18 %, found: C 71.77 %, H 8.10 %.

4,4''-Bis(2,3-dihydroxypropyloxy)-3-undecyloxy-p-terphenyl A11

Purified by crystallization from i-PropOH; yield 73 %; colorless solid; C₃₅H₄₈O₇, M=580.75 g/mol; ¹H-NMR (DMSO-D₆, J/Hz, 400 MHz) δ = 7.66-7.63 (m, 4H, Ar-H), 7.60 (d, ³J(H,H) = 8.7, 2H, Ar-H), 7.21 (d, ⁴J(H,H) = 1.9, 1H, Ar-H), 7.18 (dd, ³J(H,H) = 8.3, ⁴J(H,H) = 1.9, 1H, Ar-H), 7.01 (t, ³J(H,H) = 8.1, 3H, Ar-H), 4.21-3.95 (m, 4H, OCH, OCH₂), 3.90-3.85 (m, 2H, OCH₂), 3.81-3.75 (m, 2H, OCH₂), 3.46-3.40 (m, 4H, OCH₂), 1.70 (tt, ³J(H,H) = 6.8, ³J(H,H) = 7.5, 2H, OCH₂CH₂), 1.41 (m, 2H, OCH₂CH₂CH₂), 1.34-1.21 (m, 14H, CH₂), 0.81 (t, ³J(H,H) = 6.4, 3H, CH₃). ¹³C-NMR (DMSO-D₆, 100 MHz) δ = 158.3, 148.8, 148.3, 138.2, 138.0, 132.7, 131.8, 127.4, 126.6, 126.3, 118.8, 114.9, 114.4, 112.3, 70.6, 69.9, 69.9, 69.7, 66.5, 62.8, 62.7, 31.2, 29.0, 28.8, 28.7, 28.6, 25.4, 22.0, 13.9. Analysis: calcd. for C₃₅H₄₈O₇: ber.: C 72.38 %, H 8.33 %, found: C 72.21 %, H 8.25 %.

4,4''-Bis(2,3-dihydroxypropyloxy)-3-dodecyloxy-p-terphenyl A12

Purified by crystallization from MeOH/THF; yield 81 %; colorless solid; C₃₆H₅₀O₇, M=594.78 g/mol; ¹H-NMR (DMSO-D₆, J/Hz, 400 MHz) δ = 7.64 (d, ⁴J(H,H) = 3.7, 4H, Ar-H), 7.59 (d, ³J(H,H) = 8.9, 2H, Ar-H), 7.21 (d, ⁴J(H,H) = 2.3, 1H, Ar-H), 7.18 (dd, ³J(H,H) = 8.3, ⁴J(H,H) = 2.3, 1H, Ar-H), 7.01 (t, ³J(H,H) = 8.1, 3H, Ar-H), 4.92 (d, ³J(H,H) = 5.0, 1H,

OH), 4.83 (d, $^3J(\text{H,H}) = 5.2$, 1H, OH), 4.63 (t, $^3J(\text{H,H}) = 5.4$, 1H, OH), 4.56 (t, $^3J(\text{H,H}) = 5.8$, 1H, OH), 4.05-3.95 (m, 4H, OCH, OCH₂), 3.90-3.85 (m, 2H, OCH₂), 3.80-3.75 (m, 2H, OCH₂), 3.45-3.42 (m, 4H, OCH₂), 1.70 (tt, $^3J(\text{H,H}) = 6.8$, $^3J(\text{H,H}) = 7.7$, 2H, OCH₂CH₂), 1.41 (m, 2H, OCH₂CH₂CH₂), 1.37-1.20 (m, 16H, CH₂), 0.81 (t, $^3J(\text{H,H}) = 6.6$, 3H, CH₃). ¹³C-NMR (DMSO-D₆, 100 MHz) $\delta = 158.9, 149.4, 148.9, 138.7, 138.6, 133.3, 132.4, 128.0, 127.2, 126.9, 119.4, 115.5, 115.2, 113.0, 71.4, 70.6, 70.6, 70.3, 69.2, 63.5, 63.3, 31.9, 29.7, 29.6, 29.6, 29.5, 29.4, 29.3, 26.1, 22.7, 14.6$. Analysis: calcd. for C₃₆H₅₀O₇: C 72.70 %, H 8.47 %, found: C 72.51 %, H 8.42 %.

4,4''-Bis(2,3-dihydroxypropyloxy)-3-tridecyloxy-p-terphenyl A13

Purified by crystallization from MeOH/THF; yield 83 %; colorless solid; C₃₇H₅₂O₇, M=608.80 g/mol; ¹H-NMR (DMSO-D₆, J/Hz, 400 MHz) $\delta = 7.69-7.64$ (m, 4H, Ar-H), 7.62 (d, $^3J(\text{H,H}) = 8.7$, 2H, Ar-H), 7.24 (d, $^4J(\text{H,H}) = 2.1$, 1H, Ar-H), 7.20 (dd, $^3J(\text{H,H}) = 8.3$, $^4J(\text{H,H}) = 2.1$, 1H, Ar-H), 7.04 (t, $^3J(\text{H,H}) = 8.3$, 3H, Ar-H), 4.07-3.98 (m, 4H, OCH, OCH₂), 3.93-3.88 (m, 2H, OCH₂), 3.82-3.78 (m, 2H, OCH₂), 3.51-3.45 (m, 4H, OCH₂), 1.73 (tt, $^3J(\text{H,H}) = 7.1$, $^3J(\text{H,H}) = 7.7$, 2H, OCH₂CH₂), 1.44 (m, 2H, OCH₂CH₂CH₂), 1.32-1.23 (m, 18H, CH₂), 0.84 (t, $^3J(\text{H,H}) = 6.4$, 3H, CH₃). ¹³C-NMR (DMSO-D₆, 100 MHz) $\delta = 158.2, 148.7, 148.2, 138.0, 137.9, 132.6, 131.7, 127.3, 126.5, 126.2, 118.7, 114.8, 114.4, 112.3, 70.6, 69.9, 69.8, 69.6, 68.5, 62.8, 62.6, 31.2, 28.9, 28.9, 28.9, 28.8, 28.7, 28.6, 25.4, 22.0, 13.8$. Analysis: calcd. for C₃₇H₅₂O₇: C 72.99 %, H 8.61 %, found: C 72.81 %, H 8.60 %.

4,4''-Bis(2,3-dihydroxypropyloxy)-3-tetradecyloxy-p-terphenyl A14

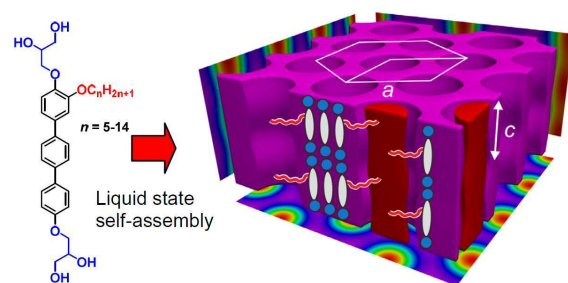
Purified by crystallization from MeOH/THF; yield 81 %; colorless solid; C₃₈H₅₄O₇, M=622.83 g/mol; ¹H-NMR (DMSO-D₆, J/Hz, 400 MHz) $\delta = 7.69-7.64$ (m, 4H, Ar-H), 7.62 (d, $^3J(\text{H,H}) = 8.7$, 2H, Ar-H), 7.24 (d, $^4J(\text{H,H}) = 2.1$, 1H, Ar-H), 7.20 (dd, $^3J(\text{H,H}) = 8.3$, $^4J(\text{H,H}) = 2.1$, 1H, Ar-H), 7.03 (t, $^3J(\text{H,H}) = 8.3$, 3H, Ar-H), 4.94 (d, $^3J(\text{H,H}) = 5.2$, 1H, OH), 4.86 (d, $^3J(\text{H,H}) = 5.2$, 1H, OH), 4.66 (t, $^3J(\text{H,H}) = 5.8$, 1H, OH), 4.58 (t, $^3J(\text{H,H}) = 5.6$, 1H, OH), 4.07-3.98 (m, 4H, OCH, OCH₂), 3.93-3.88 (m, 2H, OCH₂), 3.82-3.79 (m, 2H, OCH₂), 3.50-3.44 (m, 4H, OCH₂), 1.72 (tt, $^3J(\text{H,H}) = 6.8$, $^3J(\text{H,H}) = 7.5$, 2H, OCH₂CH₂), 1.43-1.41 (m, 2H, OCH₂CH₂CH₂), 1.32-1.22 (m, 2H, CH₂), 0.83 (t, $^3J(\text{H,H}) = 6.4$, 3H, CH₃). ¹³C-NMR (DMSO-D₆, 100 MHz) $\delta = 158.4, 148.9, 148.4, 138.2, 138.1, 132.7, 131.9, 127.5, 126.7, 126.4, 118.9, 115.0, 114.6, 112.5, 70.8, 70.1, 70.0, 69.8, 68.7, 63.0, 62.8, 31.4, 29.2, 29.1, 29.1, 29.0, 28.9, 28.8, 25.6, 22.2, 14.0$. Analysis: calcd. for C₃₈H₅₄O₇: C 73.28 %, H 8.74 %, found: C 73.15 %, H 8.66 %.

4. References

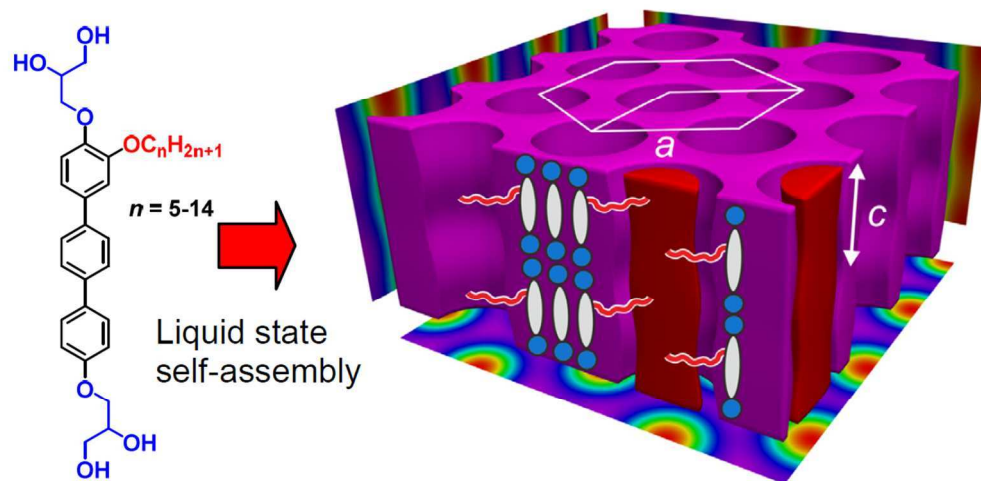
-
- S1 S. Lagerwall, A. Dahlgren, P. Jägemalm, P. Rudquist, K. D'have, H. Pauwels, R. Dabrowski, W. Drzewinski; *Adv. Funct. Mater.* 2001, 11, 87-94.
 S2 A. Immirizi, B. Perini, *Acta Cryst.*, 1977, A33, 216-218.
 S3 A. I. Kitaigorodski, *Molekülkristalle*, Akademie-Verlag: Berlin, Germany, 1979.
 S4 V. VanRheenen, D. Y. Cha, W. M. Hartley, *Org. Synth.*, 1979, 58, 43.
 S5 M. Kitamura, M. Isobe, Y. Ischikawa, T. Goto, *J. Am. Chem. Soc.* 1984, 106, 3252-3257.
 S6 a) A. Suzuki, N. Miyaura, *J. Chem. Soc., Chem. Commun.*, 1979, 866-867; b) N. Miyaura, T. Yanagi, A. Suzuki, *Synth. Commun.*, 1981, 11, 513-519.
 S7 K. Kindler, W. Peschke, *Justus Liebig's Ann. Chem.*, 1932, 497, 193-200.

-
- S8 van Rijsbergen, R., Anteunis, M. J. O., De Bruyn, A. *J. Carbohydr. Chem.* **198**, *32*, 395-404.
- S9 M. Kölbel, T. Beyersdorff, X. H. Cheng, C. Tschierske, J. Kain, S. Diele, *J. Am. Chem. Soc.* **2001**, *123*, 6809-6818.
- S10 S. J. Richards, T. W. von Geldern, P. Jacobson, D. Wilcox, P. Nguyen, L. Öhman, M. Österlund, B. Gelius, M. Grynfarb, A. Goos-Nilsson, J. Wang, S. Fung, M. Kalmanovich, *Bioorg. Med. Chem. Lett.* **2006**, *16*, 6086-6090. However, no data were given for this compound.

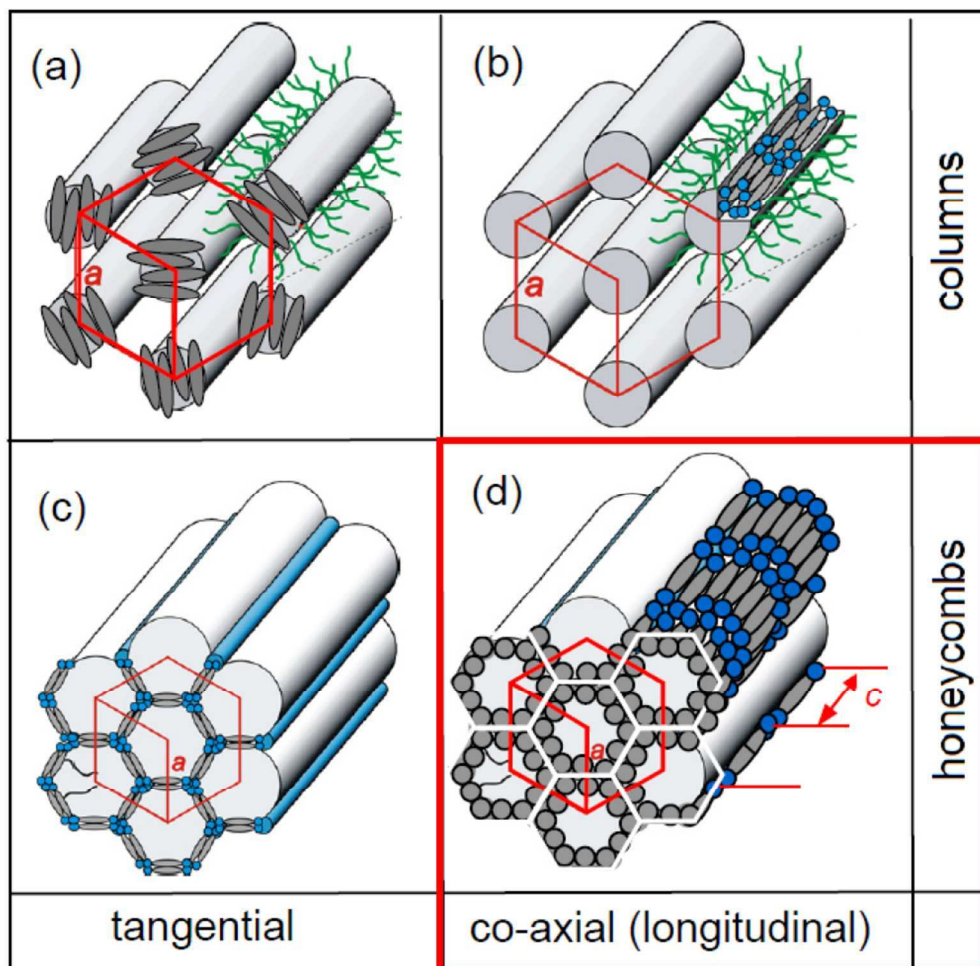
TOC



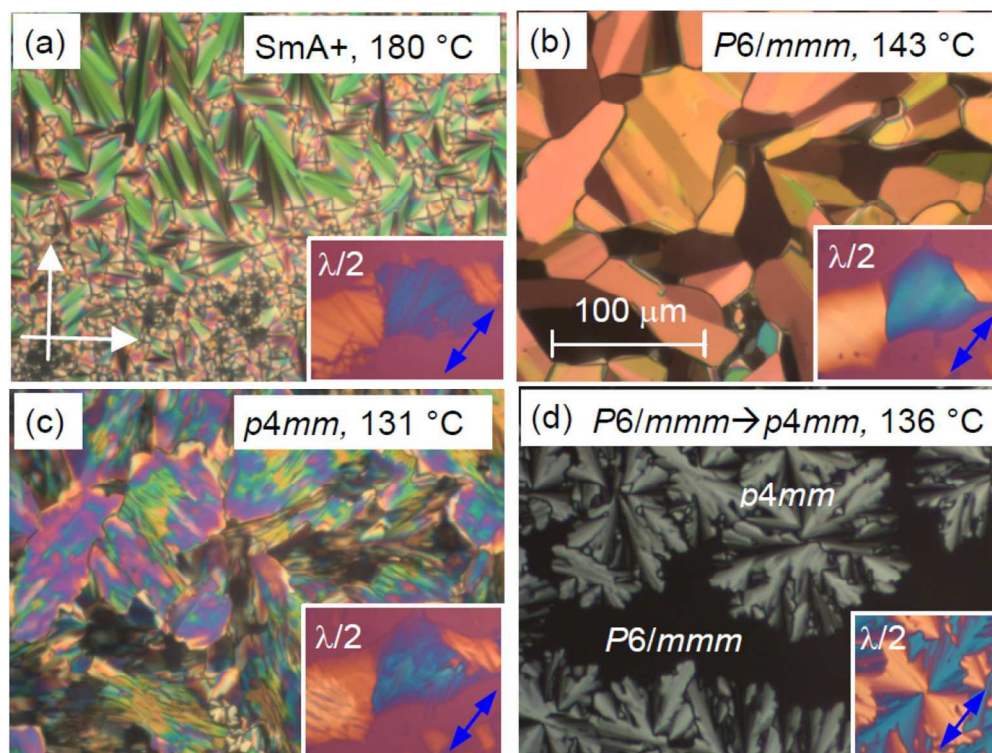
A new liquid crystalline honeycomb with an organization of π -conjugated rods parallel to the honeycomb cells is formed by molecular self-assembly.



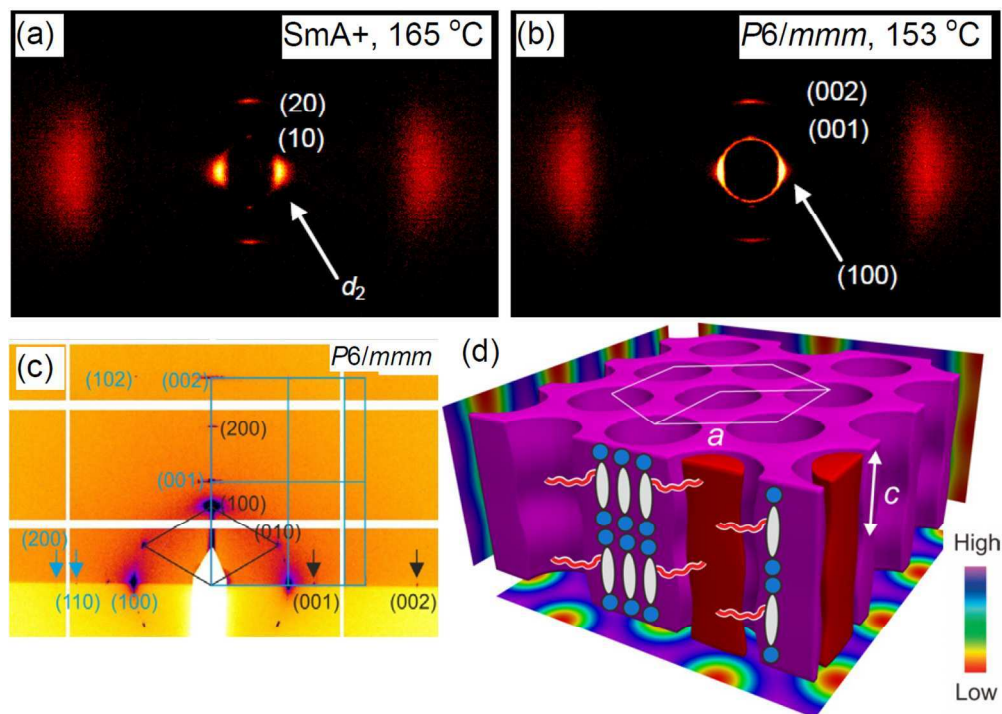
432x215mm (72 x 72 DPI)



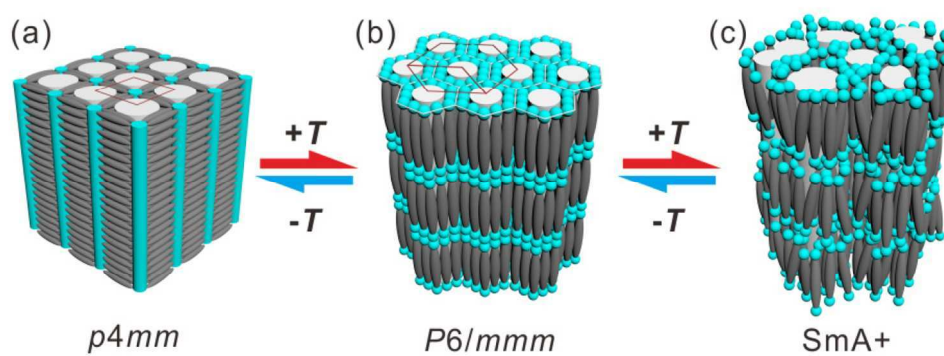
357x351mm (72 x 72 DPI)



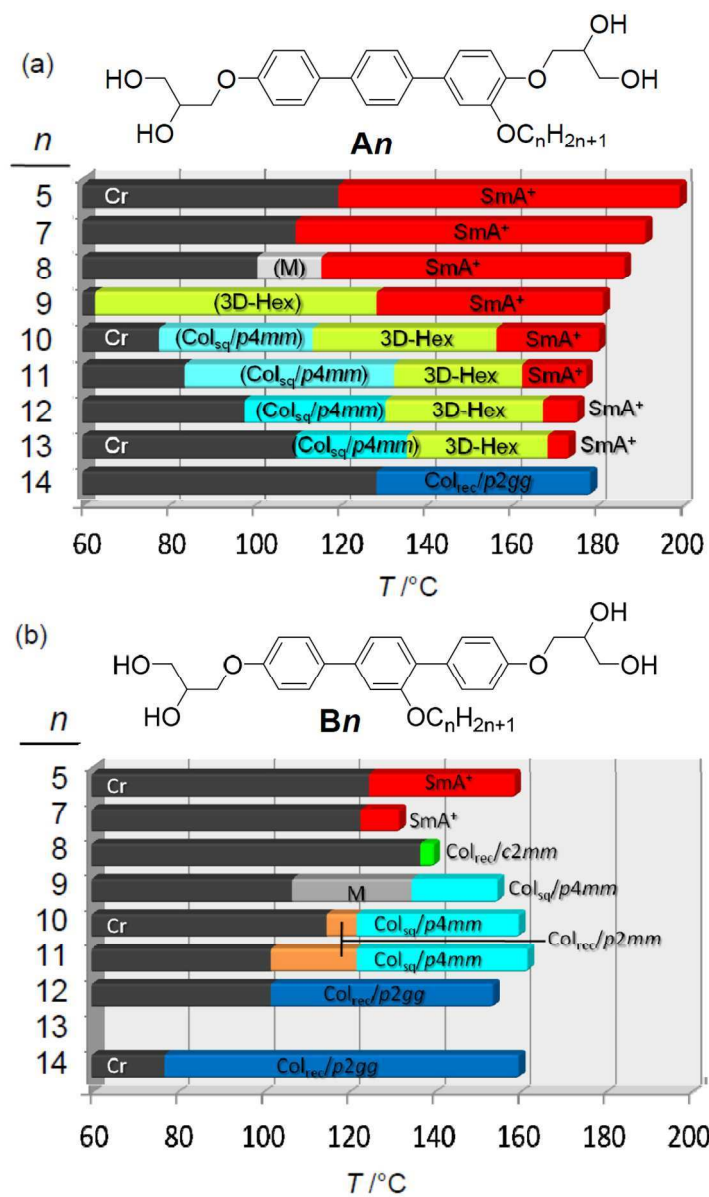
457x346mm (72 x 72 DPI)



510x368mm (72 x 72 DPI)



497x183mm (72 x 72 DPI)



395x654mm (72 x 72 DPI)